UNESCO Chair on
Coastal Geo-Hazard Analysis
Research Institute for Earth Sciences
Geological Survey of Iran
unesco
Chair

Abstract

The Astara fault system, with about 110km length and a N-S direction, and westwards dipping, is situated in the border of the Talesh mountains (in the west), and coastal part of the Caspian Sea.

Morphometric measured parameters are included: Mountain front sinuosity (Smf), ratio of valley floor width to valley height (Vf), Assymetri factor (Af), Hyposometric curve (Hi), Drainage basin shape (Bs) and transverse topographic symmetry factor (T).

The Astara fault, consists of two strike-slip and thrust components. Measured maximum and minimum horizontal displacements are about 1000 and 120 meters in Lissar and Jokandan regions.

ISBN : 978-622-8423-11-1

9 786228 423111

2024

unesco
Chair
UNESCO Chair on
Coastal Geo-Hazard Analysis
Research Institute for Earth Sciences
Geological Survey of Iran

UNESCO Chair on
Coastal Geo-Hazard Analysis
Research Institute for Earth Sciences
Geological Survey of Iran
unesco
Chair

Investigating the geometry and mechanism of the Astara fault based on the morphometric studies and Subsurface data

UCCGHA 023

2024

Investigating the geometry and mechanism of the Astara fault based on the morphometric studies and Subsurface data

سرشناسه	:	میرزایی، میترا، ۱۳۶۶- Mirzaei, Mitra, 1987-
عنوان و نام پدیدآور	:	Investigating the geometry and mechanism of the Astara fault based on the morphometric studies and Subsurface data[Book]/ authors Mitra Mirzaei; supervisors Hamid Nazari, Manouchehr Ghorashi, Ameneh Kaveh; summarized and translated into English Manouchehr Ghorashi; employer Research Institute for Earth Sciences, Geological survey of Iran; with cooperation UNESCO Chair on Coastal Geo-Hazard Analysis.
مشخصات نشر	:	تهران: خزه، ۱۴۰۳= ۲۰۲۴م.
مشخصات ظاهری	:	q، ۱۶۲ص.: مصور (رنگی)، جدول (رنگی)، نمودار (رنگی)؛ ۱۴ × ۲۱ سم.
شابک	:	978-622-8423-11-1
وضعیت فهرست نویسی	:	فیپا
یادداشت	:	زبان: انگلیسی.
یادداشت	:	عنوان به فارسی: بررسی هندسه و سازوکار گسل آستارا بر مبنای مطالعات مورفومتریک و داده های زیرسطحی.
یادداشت	:	کتابنامه:ص. ۱۶۲.
موضوع	:	گسله‌ها – مورفومتری – داده زیر سطحی -- آستارا -- ایران
موضوع	:	Faults (Geology) -- Iran -- Astara
شناسه افزوده	:	نظری، حمید، ۱۳۴۶-، ناظر
شناسه افزوده	:	Nazari, Hamid, 1968-
شناسه افزوده	:	قرشی، منوچهر، ۱۳۲۰-، ناظر، مترجم
شناسه افزوده	:	Ghorashi, Manouchehr, 1941
شناسه افزوده	:	کاوه‌فیروز، آمنه، ۱۳۶۲-، ناظر
شناسه افزوده	:	Kaveh Firouz, Amenaeh, 1983-
شناسه افزوده	:	یونسکو. کرسی مخاطرات زمین شناختی ساحلی
شناسه افزوده	:	UNESCO Chair on Coastal Geo-Hazard Analysis
شناسه افزوده	:	سازمان زمین‌شناسی و اکتشافات معدنی کشور. پژوهشکده علوم زمین
شناسه افزوده	:	Geological Survey & Mineral Exploration of Iran. Institute of Earth Sciences
رده بندی کنگره	:	۵/QE۶۰۶
رده بندی دیویی	:	۷۸۲۰۹۵۵۲۳۶۶/۵۵۱
شماره کتابشناسی ملی	:	۹۷۱۹۳۷۳

Investigating the geometry and mechanism of the Astara fault based on the morphometric studies and Subsurface data

Author:

Mitra Mirzaei

نشرخزه

اطلاعات گزارش

عنوان: بررسی هندسه و سازوکار گسل آستارا بر مبنای مطالعات مورفومتریک و داده های زیرسطحی

مجری: پژوهشکده علوم زمین، سازمان زمین‌شناسی و اکتشافات معدنی کشور

زبان مرجع: فارسی

خروجی: گزارش، نقشه، مقاله، داده های الکترونیکی

ناظران علمی: حمید نظری، منوچهر قرشی، آمنه کاوه

نویسندگان: میترا میرزایی

رئیس کرسی یونسکو در مخاطرات زمین شناختی ساحلی: حمید نظری

مسئول شورای اجرایی: راضیه لک

خلاصه‌نویسی و ترجمه به انگلیسی: منوچهر قرشی

خلاصه شده از: طرح مخاطرات زمین شناسی دریایی حوضه جنوب کاسپین

ناشر: نشر خزه

با همکاری کرسی یونسکو در مخاطرات زمین شناختی ساحلی

چاپ اول: ۱۴۰۳

شمارگان: ۵۰ نسخه

صفحات: ۱۶۲

شابک: ۹۷۸-۶۲۲-۸۴۲۳-۱۱-۱

khazepub@gmail.com

Report Information

Title: Investigating the geometry and mechanism of the Astara fault based on the morphometric studies and Subsurface data

Employer: Research Institute for Earth Sciences, Geological survey of Iran

Original language: Persian

Output: Report, Map, Paper, Digital Meta Data

Supervisors: Hamid Nazari, Manouchehr Ghorashi, Ameneh Kaveh

Authors: Mitra Mirzaei

Chairholder in the UNESCO Chair on Coastal Geo-Hazard Analysis: Hamid Nazari

Head of the Executive Council: Razyeh Lak

Summarized and translated into English: Manouchehr Ghorashi

Summarized after: Geohazard South Caspian Carpet (GSCC)

Publisher: Khazeh Publication

with cooperation UNESCO Chair on Coastal Geo-Hazard Analysis

First Edition: 2024

Edition number: 50

Page: 162

Shabak: 978-622-8423-11-1

khazepub@gmail.com

Scientific Council

Name	Affiliation
Ara Avagyan	IGS: Institute Geological Sciences
Rick J Bailey	IOC-UNESCO Indian Ocean Tsunami Warning and Mitigation System/ UNESCO
Aram Fathian Baneh	University of Calgary
Wenjiao Xiao	Chinese Academy of Sciences
Magdi Guirguis	Institut français d'archéologie orientale du Caire
Richard Walker	University of Oxford
Philippe Agard	University of Sorbonne
Justin Ahanhanzo	Intergovernmental Oceanographic Commission of UNESCO (IOC-UNESCO)
Alice Aurelie	UNESCO Water Sciences Division
Eric Barrier	University of Sorbonne
Jean-François Ritz	University of Montpellier
Martin Hanz	German under water archaeology association
Klaus Reicherter	Aachen University
Judith Thomalsky	German Archaeological Institute Tehran Branch
Hamid Alizadeh Lahijani	Iranian National Institute for Oceanography and Atmospheric

	Science
Abbas Banj Shafiei	Urmia University
Yahya Djamour	Shahid Beheshti University (SBU)
Behrouz Abtahi	Shahid Beheshti University (SBU)
Hassan Fazeli Nashli	University of Tehran
Razyeh Lak	Research Institute for Earth Sciences
Mohammad Mokhtari	International Institute of Earthquake Engineering and Seismology
Hamid Nazari	Research Institute for Earth Sciences
Jafar Omrani	Geological Survey of Iran
Morteza Talebian	Research Institute for Earth Sciences
Mohammad Tatar	International Institute of Earthquake Engineering and Seismology
Alireza Zarasvandi	Iranian Research Organization for Science & Technology (IROST) – Ministry of Science, Research & Technology
Mahdi Zare	International Institute of Earthquake Engineering and Seismology
Stefano Salvi	National Institute of Geophysics and Volcanology (INGV)
Ryo Anma	Tokushima University
Yeong Bae Seong	Korea University
John Lambert	Deltares, UNESCO
Issa El-Hussain	Sultan Qaboos University

Ekkehard Holzbecher	German University of Technology in Oman
Egor Krasinskiy	Underwater research center Russian Geographical Society
Audemard Franck A.	Department of Geology, Central University of Venezuela

Executive Committee

Name	**Affiliation**
Nasir Ahmadi	Environmental Protection Organization of Mazandaran Province
Arash Amini	Golestan University
Alireza Amrikazemi	Scientific Coordinator, Qeshm Island UNESCO Global Geopark
Parviz Armani	Imam Khomeini International University
Ataollah Dadashpour	Geological Survey of Iran, Sari branch
Asghar Dolati	Kharazmi University
Hasan Fazelinashli	University of Tehran
Fahimeh Foroghi	Iranian National Institute for Oceanography and Atmospheric Science
Abdolazaim Ghanghormeh	Golestan University
Habibolah Ghasemi	Shahrood University of Technology
Mohammad reza Ghasemi	Research Institute for Earth Sciences
Manouchehr Ghorashi	Research Institute for Earth Sciences

Jafar Hassanpour	University of Tehran
Ataollah Kavian	Environmental Protection Organization of Mazandaran Province
Mohammadreza Kazemzadeh	Superme Audit Gourt
Razyeh Lak	Head of RIES and Executive Manager
Majid Moghadam	Iranian Research Organization for Science & Technology (IROST)
Mahmoudreza Majidifard	Research Institute for Earth Sciences
Ali Akbar Momeni	Shahrood University of Technology
Babak Moradi	Iranian National Institute for Oceanography and Atmospheric Science
Seyed Mohsen Mortazavi	Hormozgan University
Hasan Nasrollah Zadeh Saravi	Caspian Sea Ecological Research Center
Ehsan Pegah	Kharazmi University
Abdolwahed Pehpouri	Qeshm Island UNESCO Global Geopark
Ahmadreza Rabani	University of Science and Technology of Mazandaran
Mahdi Rahmanian	Shargh Daily newspaper
Ahmad Rashidi	International Institute of Earthquake Engineering and Seismology
Masoud Sadri Nasab	University of Tehran
Mohammad Salamati	Respina Company

Mohammad Tatar	International Institute of Earthquake Engineering and Seismology
Alireza Vaezi	Research Institute for Earth Sciences
Mojtaba Yamani	University of Tehran
Ahmed Hadidi	German University of Technology in Oman (GUTECH)
Secretariat	
Name	**Affiliation**
Elnaz Aghaali	Research Institute for Earth Sciences
Keivan Ajdari	Research Institute for Earth Sciences
Hourieh AliBeygi	Research Institute for Earth Sciences
Sedigheh Ghanipour	Research Institute for Earth Sciences
Hamoon Memarian	Research Institute for Earth Sciences
Shirin Safavi	Research Institute for Earth Sciences
Aazam Takhtchin	Research Institute for Earth Sciences
Mehrnoosh Pour Saeid	Graphic Designer
Hanieh Bakhshaei	Geological Survey of Iran
Reza Behbahani	Geological Survey of Iran
Javad Darvishi khatooni	Geological Survey of Iran
Mohammadreza Ensani	Geological Survey of Iran
Marziyeh Estrabi Ashtiyani	Geological Survey of Iran
Gholamreza Hoseinyar	Geological Survey of Iran
Mojtaba Kavianpour Sangno	Geological Survey of Iran

Contents

Table of Figures

Table of Table

ABSTRACT

The Astara fault system, with about 110km length and a N-S direction, and westwards dipping, is situated in the border of the Talesh mountains (in the west), and coastal part of the Caspian Sea.

Morphometric measured parameters are included: Mountain front sinuosity (Smf), ratio of valley floor width to valley height (Vf), Assymetri factor (Af), Hyposometric curve (Hi), Drainage basin shape (Bs) and transverse topographic symmetry factor (T).

The Astara fault, consists of two strike-slip and thrust components. Measured maximum and minimum horizontal displacements are about 1000 and 120 meters in Lissar and Jokandan regions.

Keywords:

The Astara fault system/ Morphometry indices/ sub-surface data Talesh Mountains

CHAPTER ONE

1-1-Introduction

The mountains Alborz, with a length of nearly 600 kilometers with east-west direction, which in the central part changes direction by bending towards the south, corresponds to the tectonic block, which is referred to as the Alborz block in the northern part of the Iranian plateau (Alavi-1996) (Figure *1*).

Figure 1: South Caspian structural map (Jackson et al., 2002)

This mountain range consists of strike-slip faults parallel to the mountain range with an east-northeast trend in the eastern part and a west-northwest trend in the western Alborz (Ghorashi and Arin, 2010).

The main structures of Alborz from north to south are as follows:

Northern part: The northern margin of Alborz is linear and generally steep, and its main structures are the Caspian fault and the North Alborz fault.

Central part: The highest and also the oldest rocks of the Alborz are located in this zone, between the Caspian, North Alborz and Mosha, Rudbar and Astaneh faults.

Southern part: This part of Alborz constitutes of south-deeping thrust and left-lateral strike-slip faults that generally separate the outcrops of Eocene rocks in the south from older rocks in the north.

1-2- structural features of Alborz

The structural patterns of Alborz have been discussed and investigated by many geologists. One of the oldest theories proposed about the Alborz Mountain range is the geosyncline theory. The geosynclinal theory is an out of practice theory that still sometimes use to explain the linear subsidence that is the result of compaction of layers of sedimentary rocks deposited in a basin, then compressed and deformed and raised as a mountain range together with volcanism and plutonism. Filling of a geosyncline with millions of tons of sediments in the last stages of sedimentation is accompanied by folding and faulting in the sediments. The intrusion of crystallized igneous rocks and the uplift of a region along the displacement axis of geosyncline, generally complete the history of a geosyncline, and the result will be a folded orogenic belt. Stocklin (1974) considers Alborz as a marginal anticlinorium of central Iran and believes that this mountain range cannot be an eugeosynclinal because of the Eocene volcanic activity is not limited to Alborz and in terms of structural history cannot be separated from the central Iran. He introduced the general framework of Alborz as a deep-rooted syncline with an east-west trend and stated that the northern and southern sides of this syncline are formed by several southward and northward thrust faults, respectively. The rocks that are involved in the basements are imbricated on top of each other (Figure *2*).

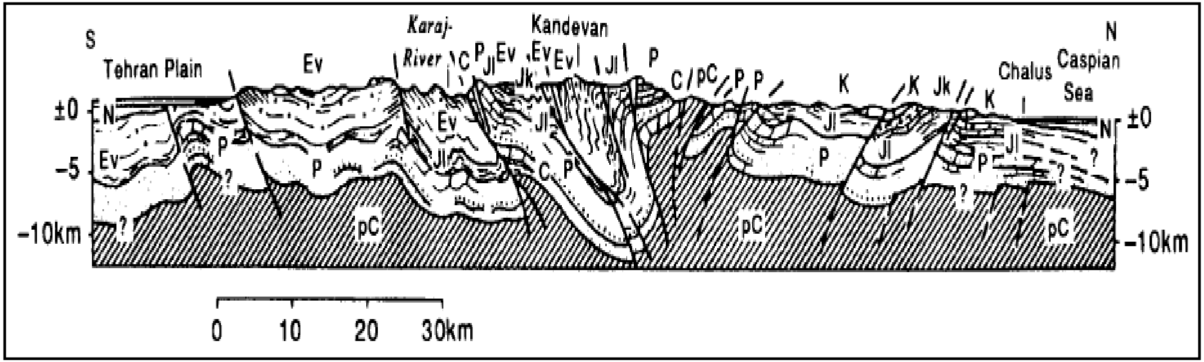

Figure 2: Cross-section of the Alborz structural framework (pC: Precambrian, C: Carboniferous, P: Permian, J1: Lower Jurassic, Jk: Jurassic and Cretaceous, k: Cretaceous, Ev: Eocene volcanic rocks, N: Neogene). (Stocklin, 1974)

Alavi (1996) considers the Alborz orogenic belt to be a thrust belt in which numerous thrust faults have thrusted several sheets from north to south. (i.l. from hinterland to the foreland)) (Figure 3). In his view, many structural sheets and duplex systems have been moved with different amounts of displacements and have created a complex form of composite antiformal stack. These structures consist of two groups of thrust systems that were created during the Cimmerian and Alpine orogenic periods, in which the Alpine structure was imposed on the Cimmerian structure and caused it to undergo renewed activity.

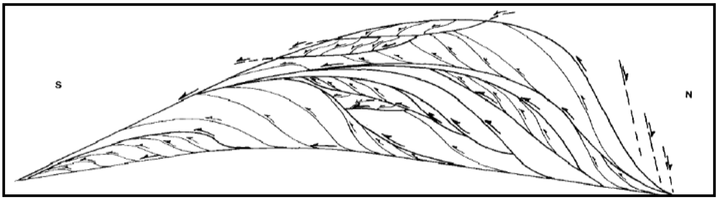

Figure 3: Structural model showing a complex duplex structure with an antiform geometry cut by low-sloping normal detachment faults. (Alavi, 1996)

According to Allen et al., (2003), the Alborz range is an excellent example of coeval strike slip and compressional deformation, and as such can be analogue for inactive fold and thrust belts though to involve a component of oblique shortening (transpressional deformation). This deformation was created as a result of the convergence of the two Arabian and Eurasian plates, with a shortening of about 30 km (Figure *4*).

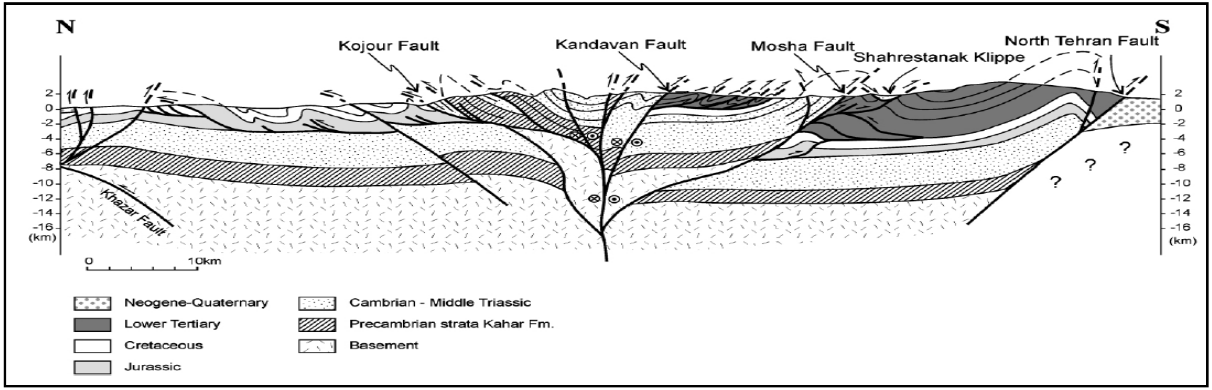

Figure 4: Structural section of Alborz, between Tehran and (Allen et al., 2003).

According to Allen et al. (2003) the Precambrian basement is not exposed anywhere in Alborz and the upper Proterozoic sediments related to the Kahar Formation are the oldest known formations in the range. The Kahar Formation passe conformably into a Cambrain-Triassic platform succession. Triassic sedimentary succession is 6Km thick in places. Stampfli, et al. (1996) suggested that an Alborz block separated from Gondwana land in the Ordovician-Silurian, and collided with Eurasia in the Late Triassic. Metamorphic relics of the Paleo-Tethyan collision are preserved in discontinuous outcrops along the northern margin of the Present range such as the Gorgan Schists. South of this metamorphic units there was widespread deposition of the Lower Jurassic, Shemshak Formation which prodominalty consists of pluvial and deltaic clastics (Figure *5*).

Marine Middle Jurassic-Early Cretaceous carbonates and clastics ware followed by Late Cretaceous carbonates, basaltic and andesitic volcanics. In the northeast, sedimentation across the Gorgan Schists began diachronously between the Early Jurassic and Late Cretaceous - Neogene clastics cover the Mesozoic strata disconformably.

Elsewhere in the range, Paleocene deposition of the Fajan conglomerate heralded the Eocene Karaj formation. This phenomenon locally reaches 5Km in thickness, and is principally exposed in the southern Alborz, where it consists of interbedded andesic volcanics and clastics.

Few Oligoncene strata are known from the Alborz, but to the south there are terrestrial red beds of this age (Lower Red Formation).

Miocene fluvial and lacustrine clastics are present in intermontane basins within and at its southern margin. Middle and upper Miocene marine clastics occur in the foothills in the northeast of the range. Evaporates are present at several Tertiary intervals to the south of the range, but not to the north.

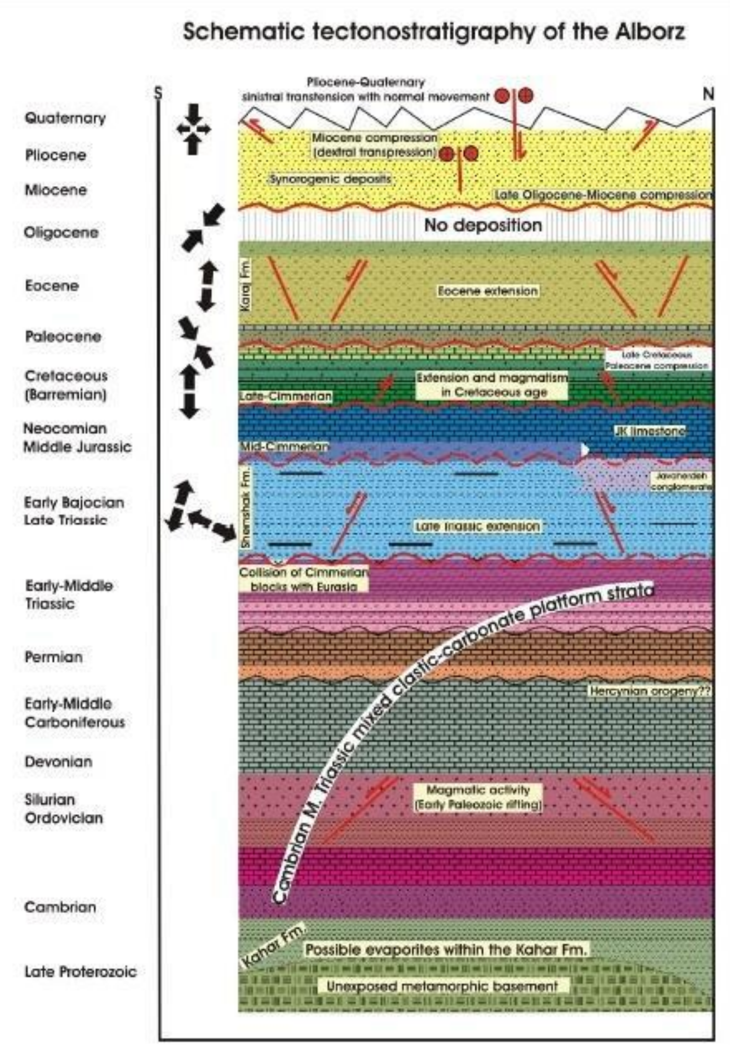

Figure 5: Alborz tectonostratigraphy model (Shahidi, 2011) and simplified tectonostratigraphy of the Alborz (Allen, 2003)

Two features of the Alborz are suprising for an active fold and thrust belt with such high relief: the young magmatism and relatively thin crust. The Alam Kuh granite was intruded at ca 7m, but no other late Miocene intrusions are Known from the range. Damavand is a unique dormant volcano within the range. Its oldest products are probably no older than Pliocene. It is enigmatic why there should be recent magmatism at all in the Alborz, and weather the Damavand and Alam Kuh centers are related. Recent magmatism occurs in other areas of Iran, such as The Sabalan and Sahand volcanoes west of the Alborz. In broad terms, all of this magmatism is likely to relate to the Arabia- Eurasia collision, The crust of the Alborz is ~35km thick (Tatar, 2001), which is no thicker than the basins to its north and south.

Zanchi et al., (2006) by analyzing the faults and ancient stress data on the Shahreshtank clip, beleive that the Eo-cimmerian tensile structures in Central Alborz have been reactivated during different phases. A N-S compressional phase that renews activity of the east-west trending faults, created folds with the same trend, during the Miocene this changed to a right-lateral transpression mechanism, which was consistent with the SW-NE direction of the maximum pressure. Zanchi et al. (2006) believe that the current tectonics of the Alborz is controlled by the left-lateral and oblique slip fault. The above structures have led to the formation of a positive flower structure (Figure *6*).

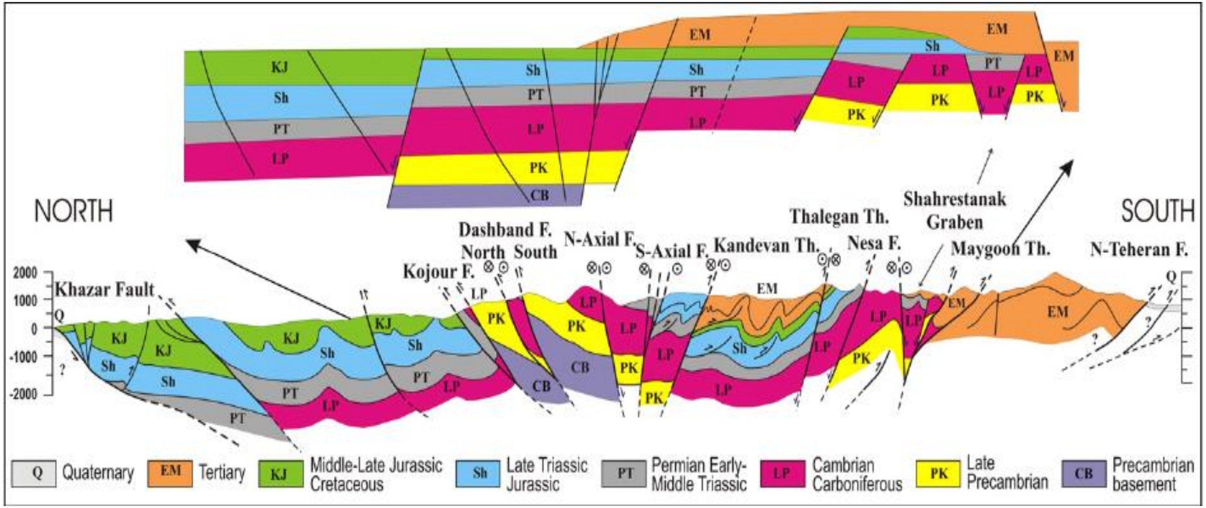

Figure 6: The cross-section of the Alborz Mountain range, (Zanchi et al., 2006), the exact location of the cross-section is shown in Figure 1.

Nazari (2006) believes that the structural evolution of the Tethys basins can be traced periodically, one after the other, among the blocks and plates such as Turan, Kopeh Dagh-Caucasus, Sabzevar, Central Iran microplate, such as Arabian plate. and the repetition of tensile and compressive tectonics resulting from the expansion and closure of these basins during the Assenitic-Katangan, Cimmerian and Alpine orogenies, which sometimes coincides with the metamorphosed and deformed basement resulting from the Caledonian and Hercynian events, has caused the tectonic evolution of the sedimentary basins that affected by various orogens. The biggest signs of the metamorphic phase of the Iranian crust can be found in the late Miocene. In the meantime, thinned Caspian crust subducted northwestward the Apsheron depositd and at the same time the oceanic crust has expanded in the Red Sea (Figure *7*). Nazari and Shahidi believe in the existence of the Rose structure in Alborz. (Figure *7* & Figure *8*).

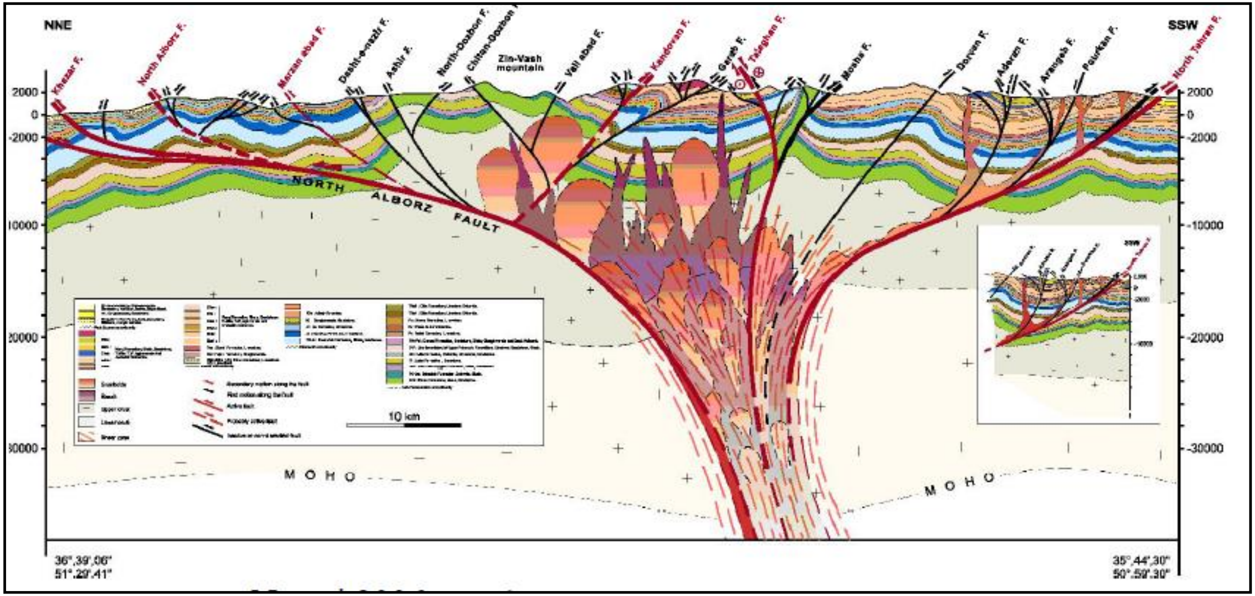

Figure 7: Structural model of Central Alborz between Karaj-Chalus section (Nazari, 2006).

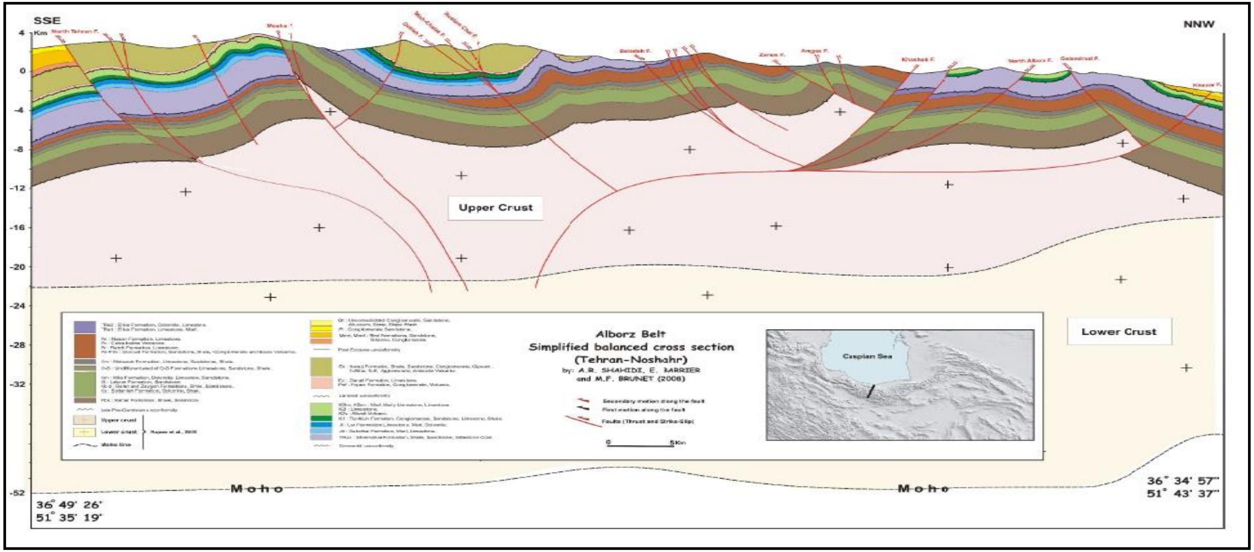

Figure 8: Structural section of Alborz, the location of the section is indicated in the small map (Shahidi, 2011).

CHAPTER TWO

MORPHOTECTONICS INVESTIGATIONS

2-1 Morphotectonics

The term “active tectonics” refer to those tectonic processes that produced deformation of the Earth′s crust on a time of significance to human society. In recent years, tectonic geomorphology is one of the major and essential effective tools in detecting active tectonic landforms and producing seismic hazard maps. In this method, by evaluating satellite images and aerial photos with high accuracy, DEM and calculation of morphotectonic indicators will find out whether the area is tectonically active or inactive.

2-1-1 Morphometry

Morphometry is defined as qualitative measurement of landscape shape. At the simplest level, landforms can be characterized in terms of their size, elevation (maximum, minimum, or average), and slope. Quantitave measurements allow geologists to objectively compare different landforms and to calculate less straightforward Parameters (geomorphic indices) that maybe useful for identifying a particular characteristic of an area for example, its level of tectonic activity.

Some of the geomorphic indices most useful in studies of active tectonics are:

- Drainage Basin shape indicator (Bs)
- Hypsometric integral (Hi)
- Drainage basin Asymmetry Factor (AF)
- Mountain Front Sinuosity (Smf)
- Transverse Topographic Symmetry Factor (T) of the drainage basin
- Ratio of Valley-Floor Width to Valley Height (Vf)

The results of several of the indices may also be combined, along with other information such as uplift rates, to produce tectonic activity class, and relative activity in area.

2-1-1-1 Shape of the drainage basin (Bs).
This index is calculated through the following formula:

Bs=Bl/Bw

In this formula, Bs is the shape of the drainage basin, Bl is the length of the drainage basin, and Bw is the maximum width of the drainage basin.

This index shows the difference between long basins with high values and circular basins with low values. Long basins have been the characteristics of active tectonic areas that have rivers with downward cutting. Mountain fronts with rapid uplift, consist of long steep basins and when the tectonic activity decreases or stops, the widening of the basins starts from the upper side of the mountain front (Figure 9).

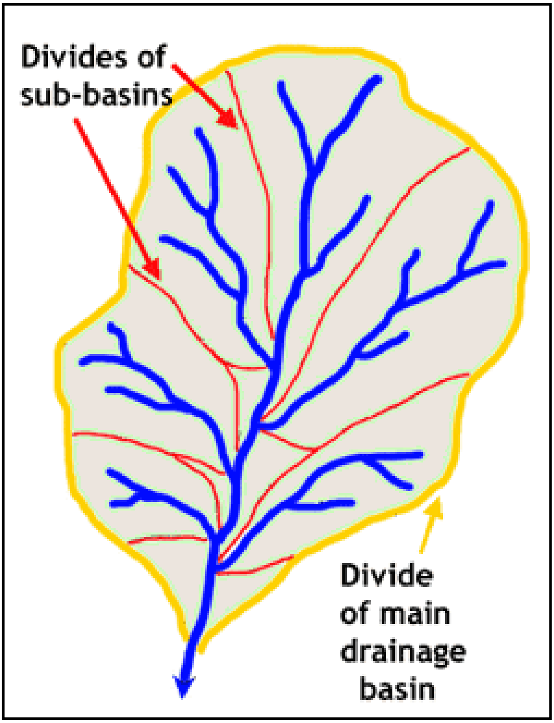

Figure 9: Idealized diagram showing Bl and BW indices

This index is obtained according to the length of the basin, which is calculated from the outlet of the basin to the highest point of the basin, on the widest width of the basin. Basins with high elongation indicating the active tectonic zones. According to Hamdouni (2007) values less than 3 is the lowest activity rate, values between 3 and 4 are mean activity rate and values greater than 4 have the highest tectonic activity rate.

2-1-1-2 Hypsometric curve and hypsometric integral

The hypsometric curve describes the distribution of elevations across an area of land, from one drainage basin to the entire planet. The curve is created by plotting the proportion of total basin height (relative height) against the proportion of total basin area (relative area) (Figure *10*). A hypsometric curve for a drainage basin on a uniform slope (Figure *11*) illustrates how the curve is created. The drainage basin spans eight contourlines, numbered 1 to 8 on the figure. The total surface area of the basin (A) is the sum of the area between each pair of adjacent contour lines. The area (a) is the surface area within the basin above a given line of elevation(h). The value of relative areas (a/A) always varies from 1.0 at the lowest point in the basin (h/H=0.0) To 0.0 at the highest point in the basin (h/H=1.0)

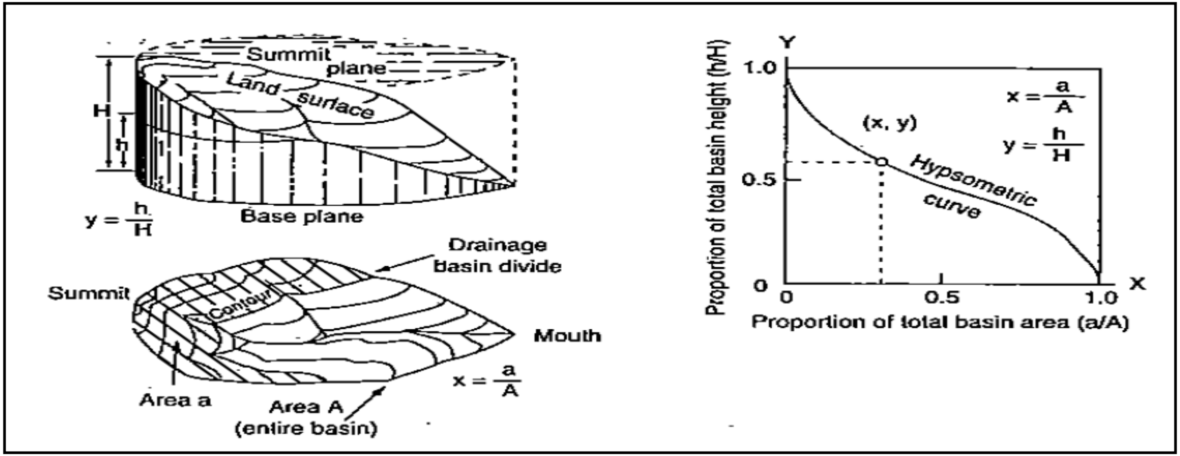

Figure 10: Hypothetical drainage basin indicating how one point (x,y) on the hypsometric curve. Plotting several 0.12 values (for different contours) of a/A and h/H allows the curve to be constructed (Keller & Pinter, 2002).

To calculate hypsometric curve, first we must create a 50 or 100 meter curve in the studied area, obtain the mentioned parameters and draw a hypsometric diagram.

A= The total area of the basin

H= is the highest height in the basin

a= is the area surface two consecutive meters and an area of the basin that is above the height h.

The relative value of a/A usually changes between the value of 1 at the lowest point of the basin (h/H=0) and the value of zero at the highest point of the basin (h/H=1). Since in the hypsometric curve, the area and height of the watershed are divided by the area and the height of the whole basin is divided and the resulting numbers are dimensionless on the curve, in this case the hypsometric curve is independent of area and height, and the hypsometric curves of drainage basins of different sizes in terms of height and area can be compared with each other. and be analyzed. Therefore, topographic maps can be used in large and small scales, and the difference in area and scale has no effect on hypsometric evaluations (Figure *11*).

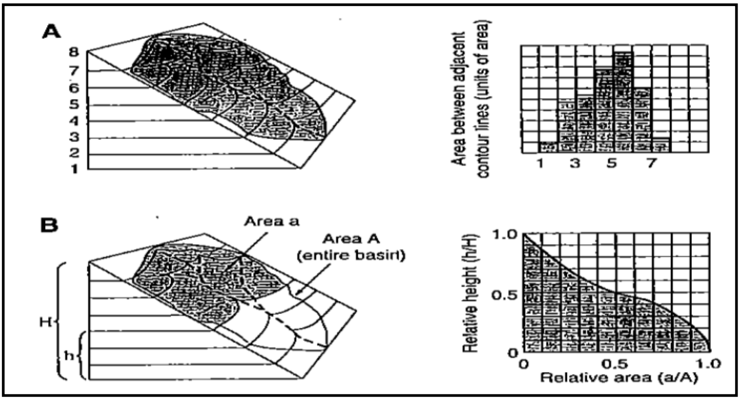

Figure 11: Ideal diagrams showing the determined hypsometric curve. (Keller & Pinter, 2002)

One of the easiest ways to characterize the shape of the hypsometric curve for a given drainage basin is to calculate the **hypsometric integral**. The hypsometric integral of the basin is determined by calculating the area under the hypsometric curve. One way to calculate the hypsometric integral for a given curve is as follows:

$$\frac{mean\ elavation - minimum\ elevation}{maximum\ elavation - minimum\ elevation}$$

The relationship between the hypsometric integral degree of dissection permits its use as an indicator of a landscap's stage in the cycle of erosion.

The cycle of erosion describes the theoretical evolution of landscape through several stages: a "youthful" stage characterizes by deep incision and rugged relief, a "mature" stage where many geomorphic operate in approximate equilibrium and an "old age” stage characterized by a landscap near base level with very subdued relief. A high hypometric integral indicates a youthful topography (Figure *12*)

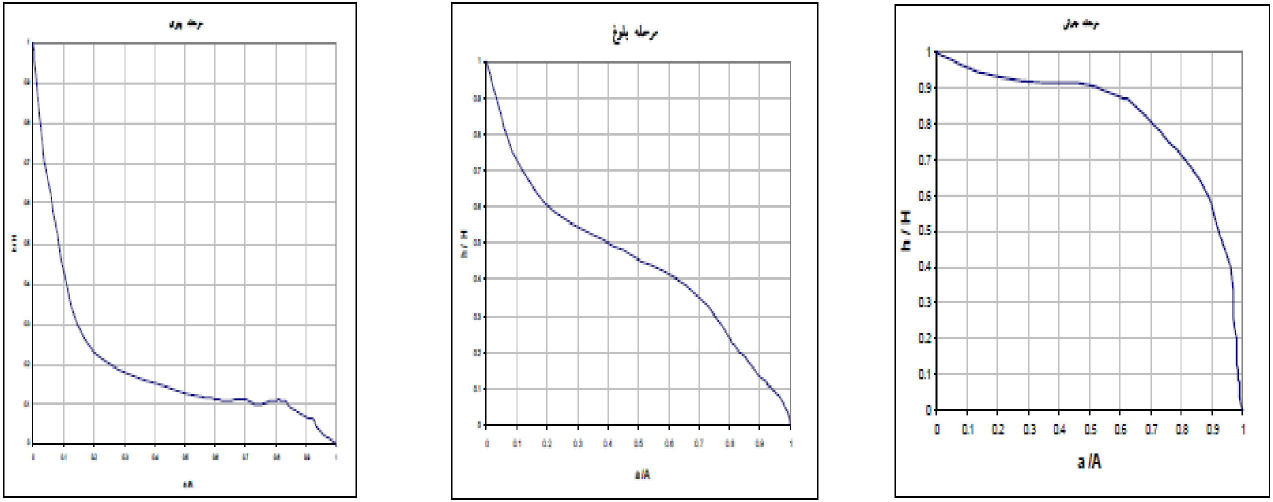

Figure 12: Three examples of different values of the hypsometric integral (Keller & Pinter, 2002).

The hypsometric values less than 0.5, indicating very low tectonic activity, if it is equal to 0.5, the tectonic activity is moderate, and value more than 0.5, the area has active tectonics (Hamdouni, 2007).

2.1.1.3- Drainage basin asymmetry

The geometry of stream networks can be described in several ways, both qualitatively and quantitatively. Where drainage develops in the presence of active tectonic deformation, the network often has a distinct pattern and geometry. The **Asymmetry Foctor** was developed to detect tectonic tilting at drainage-basin scales of larger area.

The asymmetry factor (AF) is defined as: (Figure *13*).

AF=100(Ar/At)

where Ar, is the area of the basin to the right (facing downstream) of the trunk streams and at is the total area of the drainage basin. AF Should equal abant 50. The AF is sensitive to tilting perpendicular to the trend of the trunk stream. Values of AF greater or less than 50 may suggest tilt.

Like most geomorphic indices, The AF works best where each drainage basin is underlain by the same rock type. The method also assumes that neither is lithologic control (such as dipping sedimentary layers) nor localized climates (such as vegetation differences between north and south facing slopes) causes the asymmetry.

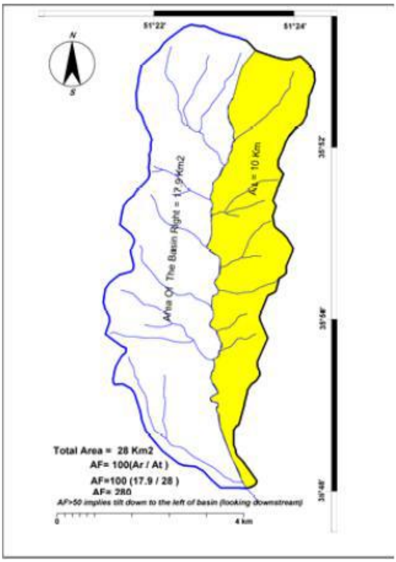

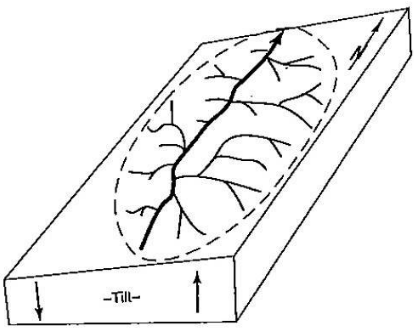

$$AF = 100\left(\frac{A_r}{A_t}\right)$$

Figure 13: Figure 2.5- Block diagram showing the measuring of tilting. The figure on the top is from Gourabi (2005), and the figure on the bottom is from Keller and Pinter (2002).

2.1.1.4 - Mountain-Front sinuosity

Mountain-front sinuosity is defined as:

$S_{mf} = L_{mf}/L_s$

where S_{mf} is the mountain front sinuosity; L_{mf} is the length of the mountain front along the foot of the mountain, of the pronounced break in slope; and L_s is the straight-line length of the Mountain front (Figure *14*). Mountain-front sinuosity is an index that reflects the balance between erosional forces that tend to cut embayments into a mountain front and tectonic forces that tend to produce a straight mountain front coincident with an active range-bounding fault. Those mountain fronts associated with active tectonics and uplift are relatively straight, with low values of S_{mf}. If the rate of uplift is reduced or ceases, then erosional processes will carve a more irregular mountain front, and S_{mf} will increase.

Based on the available data, if the values obtained are smaller than 1.53, the area is placed in tectonic class one, if it is placed between 1.8-2.3, the tectonic class will be two, and between 2.8-3.5 the tectonic class will be three.

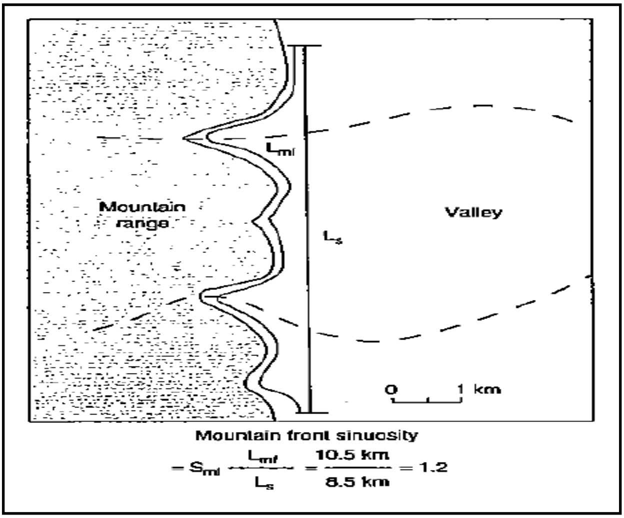

Figure 14: Idealized diagram showing how mountain-front sinuosity is calculated.

2.1.1.5 – Transverse topographic symmetry factor (t)

Another indicator of the asymmetry of the basin is the transverse topography symmetry factor, which is calculated from the following equation:

$T=D_a/D_d$

Where, D_a is the distance from the midline of the drainage basin to the midline of the active meandering belt and D_d is the distance from the basin midline of the basin (Figure *15*).

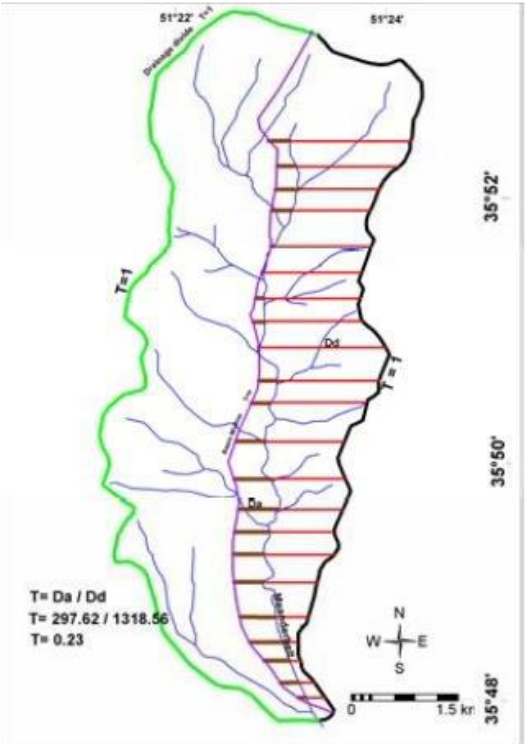

Figure 15: Evaluation of transverse topography symmetry index (Gourabi, 2005)

For a perfectly symmetrical basin, T=0. With the increase of asymmetry, the T index increases and finally approaches a value of 1. Assuming that the dip of the bedrock has a negligible influence on the migration of the main river channel, in this case, the direction of regional migration is an indication of the ground tilting in that direction. Therefore, T is a vector with a direction and magnitude (0-1). This factor is more suitable for drainage basins with a dendritic pattern. Values between from 0.1-0.4 are tectonically active in category one, numbers between 0.05-0.09 are in category two, which are tectonically moderate. and values of 0 to 0.05 are in category three, with little tectonic activity.

2-1-1-6 The ratio of valley-floor width to valley height This Index is obtained from the following relationship:

$V_f = 2V_{fw}/[(E_{ld}-E_{sc}) +(E_{rd}-E_{sc})]$

Where, V_f, is the the valley floor width to height ratio, V_{fw} is the width of the valley floor, E_{ld} and E_{rd} are evalation of the left and right of the valley divides respectively, E_{sc} is the elevation of valley floor (Figure *16* & Figure *17*).

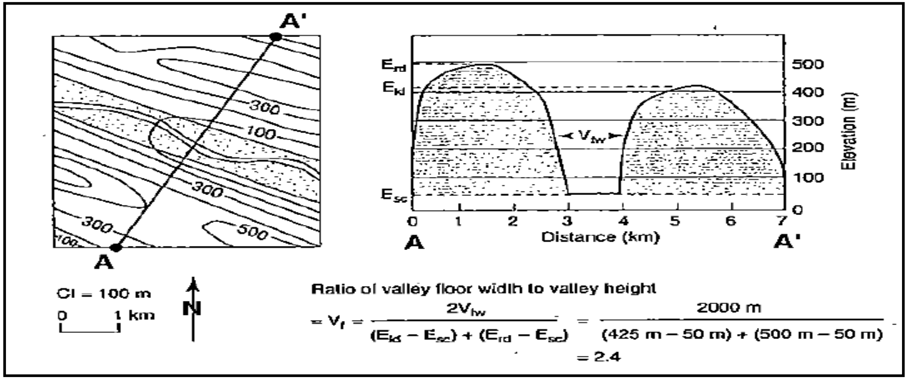

Figure 16: The idealized diagram calculation of the ratio of valley-floor with to valley height (Keller & Pinter, 2002).

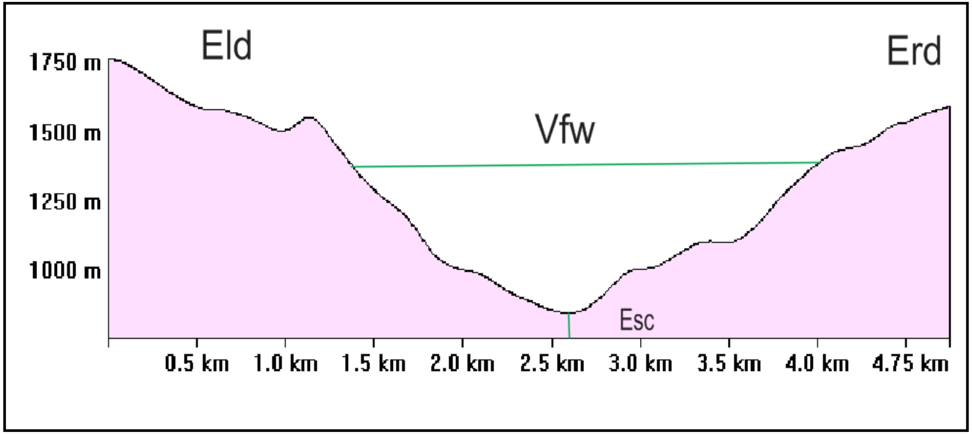

Figure 17: Elevation model of a valley to show the details of the V_f index. V_{fw} is the width of the valley, E_{sc} is the height of the valley floor and E_{ld} and E_{rd} are the heights of the dividing line of water on the left and right side of the valley.

This index differentiates between broad-floor canyons, with relatively high V_f values from V-shaped valleys with low V_f values. High values of V_f are related with low uplift rates, so that streams cut broad valley floors. Low values of V_f reflect deep valleys with streams that are actively incising, commonly associated with uplift. If the value of Vf obtained is less than 0.5, it is tectonically active, if the value obtained is between 0.5-1, tectonic activity is moderate and if it is more than 1, the valley tectonically is inactive.

2-2 Geometrical measurements of the young fault

2-2-1 Measurement of horizontal and vertical displacements (H & V)

In this method, the longitudinal and transverse displacements of the features that have significant displacements along the fault are considered. For example, a river or a waterway that passes vertically through the fault with a significant lateral movement, by creating two profiles on the river before and after the displacement and plotting these two profiles on each other, the amount of vertical displacement of the area will be obtained (Figure *18*)

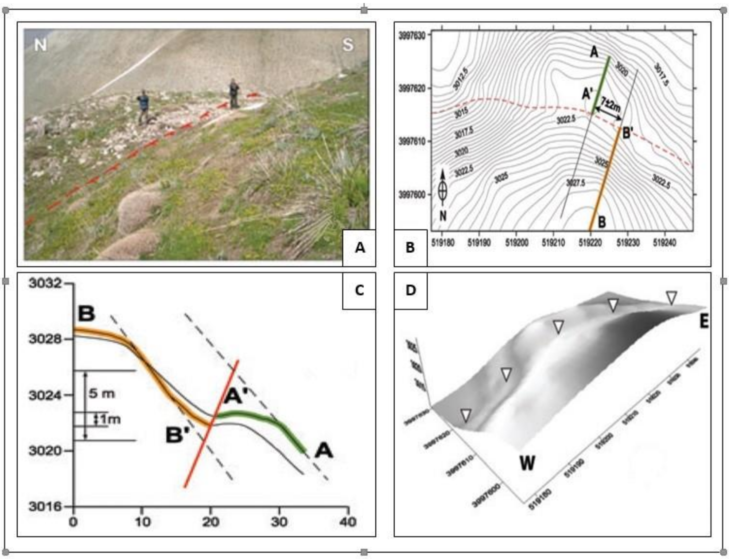

Figure 18: Calculation the vertical displacement by using a digital elevation model, A) shows the location of the fault trace. B) Topographical contours projection on both sides of the fault by which the amount of vertical displacement of the fault. C) Integration of two elevation sections obtained using Grapher4 software to calculate the vertical displacement. D) 3D map of the fault trace (white triangles) (Nazari et al. al., 2009).

2-2-2 Rake

The angle between the line that shows the effect of the fault on the surface and the horizontal line that is located on the fault surface is called rake (Figure *19*). Faults on the basis of rake angle are divided into three groups:

Dip slip fault: It is a fault where the slip angle is 90 degrees and the dip slip is equal to the total slip.

Strike-slip fault: in this case, the total slip is parallel to the fault, and there is no movement in the direction of the fault slope, and the angle of the rake slip is equal to zero.

Diagonal slip fault: In this case, the total slip angle is between 0 and 90 degrees, and there is both oblique and longitudinal slip.

How to calculate Rick is as follows:

Cos ^c = d/v
^c + ^p + ^b + 90° = 180°, ^b = 90° - ^c - ^p
Vf = d/cos ^b
^R = arctg Vf/H

C indicates the slope, P indicates the slope of the fault plane, Vf indicates the amount of displacement on the fault plane, d indicates the amount of vertical displacement, R indicates the amount of rack, H and V the horizontal and vertical displacement respectively.

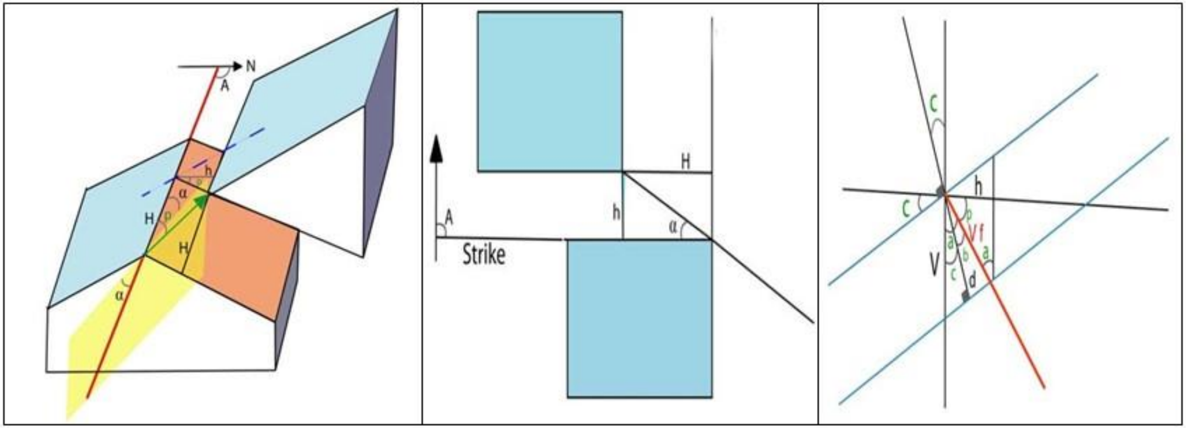

Figure 19: Block diagram that shows the method of measuring the angle of fault rake based on horizontal and vertical displacements relative to the hanging wall and the foot wall. (Nazari, 2006)

2-3 Geophysical Investigation

2-3-1 GPR method

Ground Penetrating Radar (GPR) is one of the modern geophysical methods for surveying near the ground surface. In this method, high frequency electromagnetic waves (in the megahertz range) are used to detect subsurface structures. GPR equipment reveal subsurface discontinuous with high resolution by producing and emitting discontinuous electromagnetic purposes. These pulses are produced by the signal generator and sent into the ground by different antennas. The shape and characteristics of the produced pulses are a function of the antenna characteristics that used for surveying and generally these antennas are named according to the frequency center of the produced pulse (Figure *20*).

2-3-1-1 Applications of GPR method

In general, the success of geophysical methods depends on the existence on the contrast in the physical characteristics of subsurface targets with their surrounding environment. The parameter that causes subsurface targets to be detected by GPR method is contrast in the electromagnetic characteristics of materials (electrical permeability, electrical conductivity and magnetic permeability). In most geological conditions where the conductivity and magnetic permeability of the subsurface environment can be neglected, the contrast in dielectric transmissivity has the greatest contribution in detecting subsurface targets. Therefore, in using this method, many subsurface anomalies can be detected.

The range of GPR applications is very wide and for various purposes such as determining the thickness of the soil as well as the stratigraphy of sediments, determining the level of sedimentation, detecting holes, buried channels and tunnels, detecting seams and cracks in dense rocks, mapping contaminated areas. Investigating the conditions of construction sites of huge structures, non-destructive examination of building materials, bridge columns and dam walls, determining the thickness of glaciers and various other applications. Among the positive applicability of this method, in addition to its high resolution are the speed of data collection as well as its non-invasive properties. In this way, data can be collected in urban environments without having destructive effects on the environment.

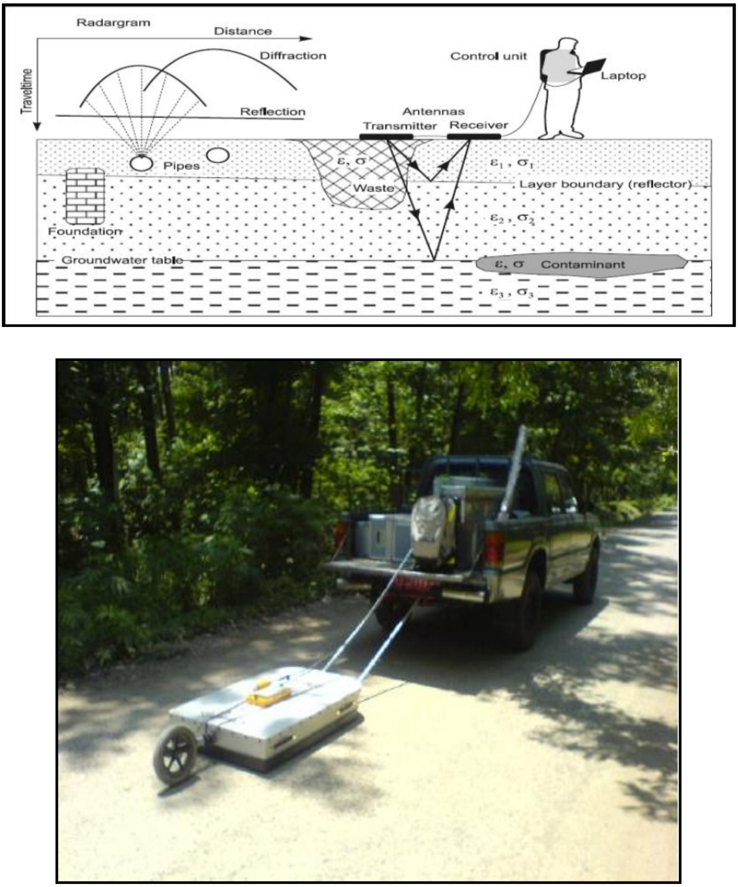

Figure 20: a and b) Schematic view of the principles of acquisition and components of the GPR.

2-3-2 Resistivity method

In this method, artificial electric currents are injected into the earth by two electrodes and the resulting potential difference between two points on the earth's surface is measured. The mean purpose of electrical methods is to measure the electrical resistivity of the earth. In order to identity a subsurface feature electrical resistance must be significantly different from the surrounding environment: Therefore, the use of electrical method is limited to cases where there is a resistivity variation. In this method, geological features, underground water and other existing features are not measured directly. But for proper interpretation of electoral data, a series of external information is needed. The electrical resistivity methods which is one of the well- known-electrical methods, is effectively used to discover underground water resources, investigate the types of groundwater pollution, reveal the location of subsurface cavities, faults and crushed zones, as well as archeological sites. The target of resistivity measurements is to determine the underground distribution of resistivity by surface measurements. In resistivity measurements, a direct electric current is sent into the ground by two current electrodes (A, B) and the resulting potential difference between the two potential electrodes (M,N) is measured in the ground. Resistivity is calculated from the formula P=K.V/I. V is the measured potential difference and I is the intensity of the current injected into the ground and K is the geometry coefficient of the array. However, the basic equation for calculating the apparent resistivity for any taype of electrode arrangement is as follows:

$$K = 2\pi . \frac{1}{\frac{1}{AM} - \frac{1}{AN} - \frac{1}{BM} + \frac{1}{BN}}$$

When the ground material is homogeneous, the resistivity calculated based on this equation is constant and independent of the distance between the electrodes, but if there is subsurface heterogeneity, the resistivity changes with the relative position of the electrodes, and each value calculated as the apparent specific resistivity will be a function of the corresponding heterogeneity.

The three arrays used in this method are:

1) dipole-dipole

2) pol-dipole

3) Wenner

2-3-3 Geomagnetism Method

About 99% of the earth's magnetic field originates from inside the earth and only one percent of it originates from outside the earth. The magnetic field F can be described by the angle of inclination and deviation. The angle of deviation D is the angle between the magnetic field vector and geographic north (Figure *21*).

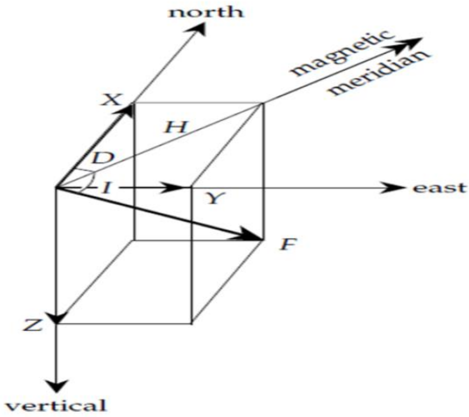

Figure 21: The components of the earth's magnetic field, F, X, and Y, are considered positive in the north and east geographical directions, and Z is considered downwards. Angles I and D are the angles of inclination and deviation of the magnetic field vector, respectively (Lowrie, 2007).

Magnetometers record the magnitude of the total magnetic field regardless of its vector direction. To study the magnetic anomalies of the crust, the magnetic anomaly is measured by subtracting the effect of the earth reference field (IGRF) from the total field.

The smaller the distance between the surveying lines, will be the higher precision of the array. The choice of this distance is affected by the wavelengths of the anomalies in the direction and perpendicular to the surveying lines and the extent of the anomaly source.

The surveying lines should be enough that detail anomalies should not be ignored (Figure 22).

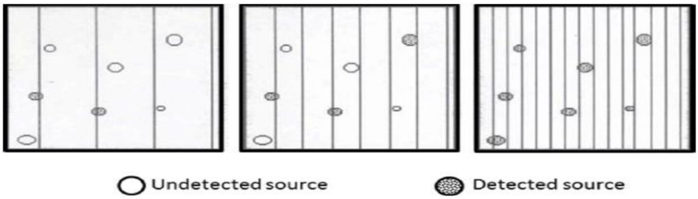

Figure 22: Three magnetic surveys with different surveying line distances. As the surveying line distance decreases, the number of undetected sources increases.

The collected data in this method consist of at least three characters Y, X (point coordinates) and Z (magnetic field intensity value at each point), which are collected discretely. To perform a series of two-dimensional processing, the data format should be continuous. The interpolation of readings at different points in order to determine the data values at the node points, is called gridding (Figure 23).

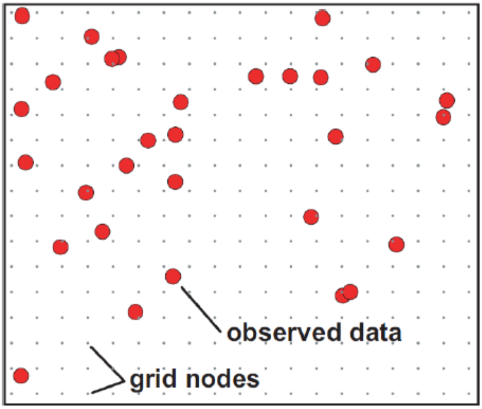

Figure 23: In the figure, the initial process of gridding is shown. The red circles are the serveyed data, the act of interpolating the data value at the node points with regular intervals is specified.

The areas that have been examined this study are Lisar, Jokandan, Gissum and Talash regions.

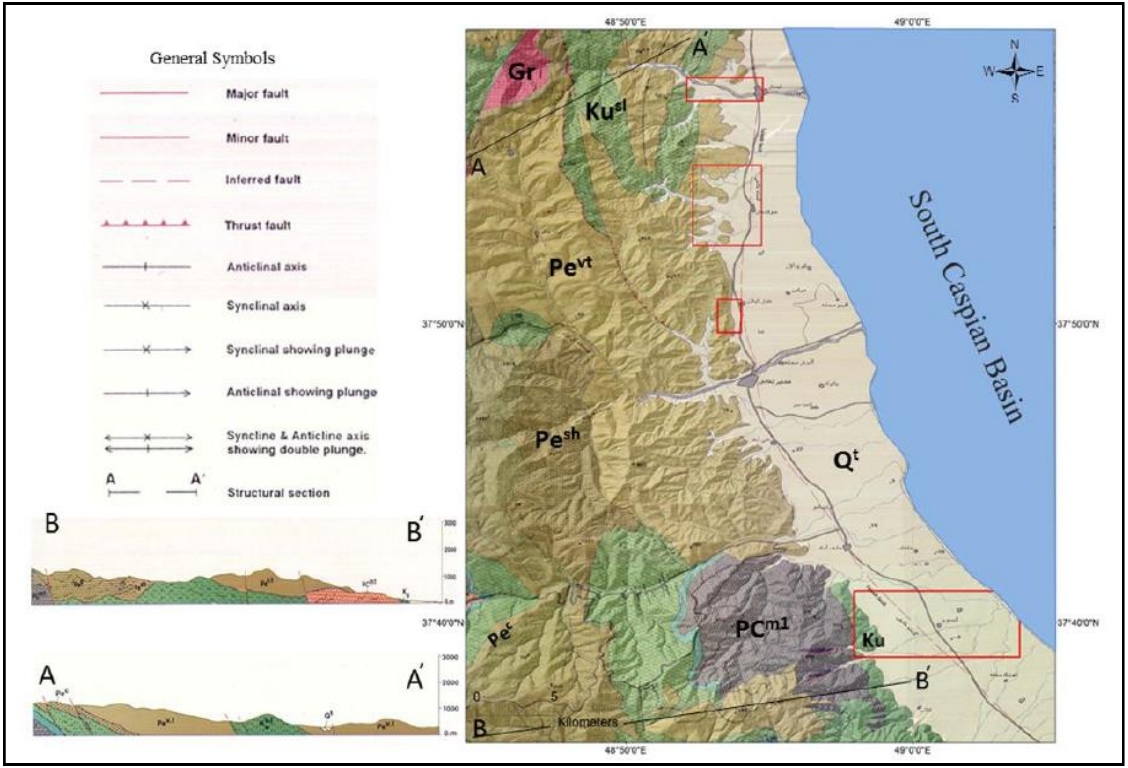
General Symbols
Major fault
Minor fault
Inferred fault
Thrust fault
Anticlinal axis
Synclinal axis
Synclinal showing plunge
Anticlinal showing plunge
Syncline & Anticline axis showing double plunge.
Structural section
South Caspian Basin
Gr
Ku^{sl}
Pe^{vt}
Pe^{sh}
Pe^{c}
PC^{m1}
Ku
Q^{t}
A
A′
B
B′
48°50'0"E
49°0'0"E
37°50'0"N
37°40'0"N
Kilometers

Figure 24: Geological map of Khalkhal sheet - Rezvanshahr on a background of DEM topographic data image (http://asterweb.jpl.nasa.gov/gdem-wist.asp) with the spatial accuracy of 30 meters. The red squares area is studied by magnetic method.

CHAPTER 3

The MORPHO - TECTONICS of the ASTARA FAULT

3-1 Introduction

Morphometry is a quantitative measurement of landscapes on the earth that can be obtained mostly by simple variables such as size, height, and slope (Bull, 2007). These data provide conditions for geologists by comparing different phenomena to identify areas with active tectonics (Keller and Pinter, 1996). The use of geomorphological indicators has become more popular in recent years due to the easily calculation and low error in detecting active areas.

In this research, in order to obtain the morphometric indices of the region, the existing basins were separated and identified into about 24 basins. Due to the large number of basins and the length of the Astara fault, the southern part, which is located from Hashtpar to Rezvanshahr, will be discussed and investigated in this research. In this regard, the basins of the southern part will start from number 17 and obtained indices of this area will be analyzed (Figure *25*).

3-2 Morphometry of the Astara fault

The geomorphological indices that are used in the evaluation of the tectonic activity of the region are examined in this part of the research. Therefore, all the factors for calculating the relevant indicators are mainly studied in one unit (Quaternary deposits) in a similar climatic condition.

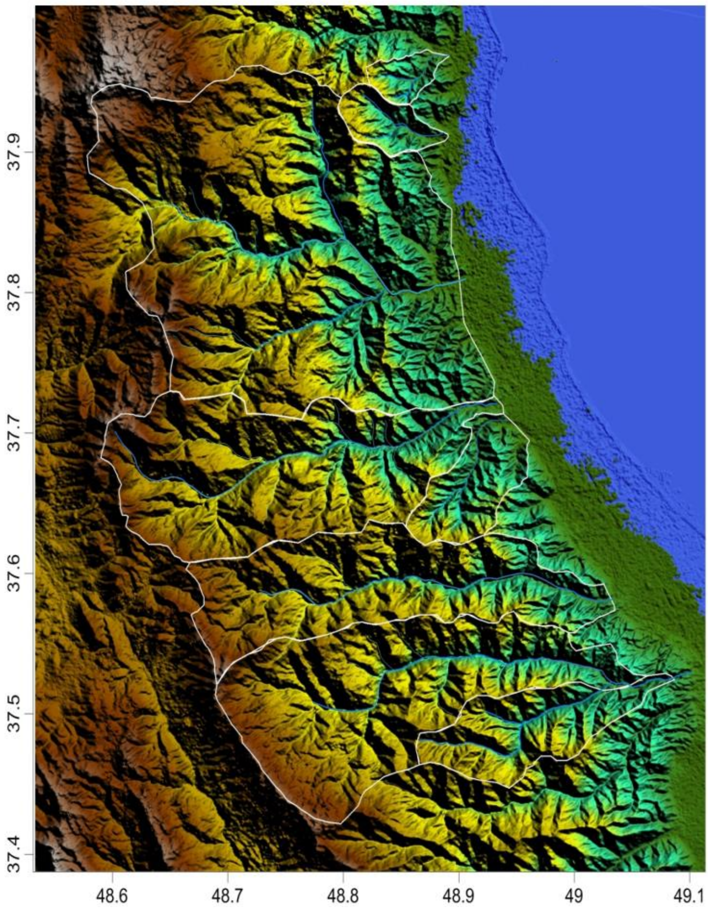

Figure 25: An overview of the studied basins in the study area. The dashed line is the approximate location of the Astara fault. The DEM background (http://asterweb.jpl.nasa.gov/gdem-wist.asp) with a spatial accuracy of 30 meters.

3-2-1: Shapes of the Drainage basin (BS)

$B_s = B_l / B_w$

This index shows the ratio of the length of the basin to the widest part of the basin. In general, basins with high elongation, tectonically are active areas, and relatively circular basins have less tectonic activity. According to Hamdouni et al., (2007) values less than 3 are in low tectonic activity class, between 3-4 are in medium tectonic class and values above 4 are in active tectonic class. (Figure *26* & Table 1).

Table 1: Bs index calculated in the research area

Drainage basin shape(Bs)				
Basins	BI(m)	Bw(m)	Bs	Tectonic Class
17	5875	3716	1.581	3(Low Activity)
18	8713	4487	1.94	3
19	32527	27988	1.16	3
20	30452	13747	2.22	3
21	11889	8754	1.358	3
22	32412	8261	3.92	2(Moderate Activity)
23	36104	14116	2.56	3
24	16050	6660	2.409	3
Bs Classification:(<3)Low Activity,(3-4)Moderaite Activity,(>4)High Activity				

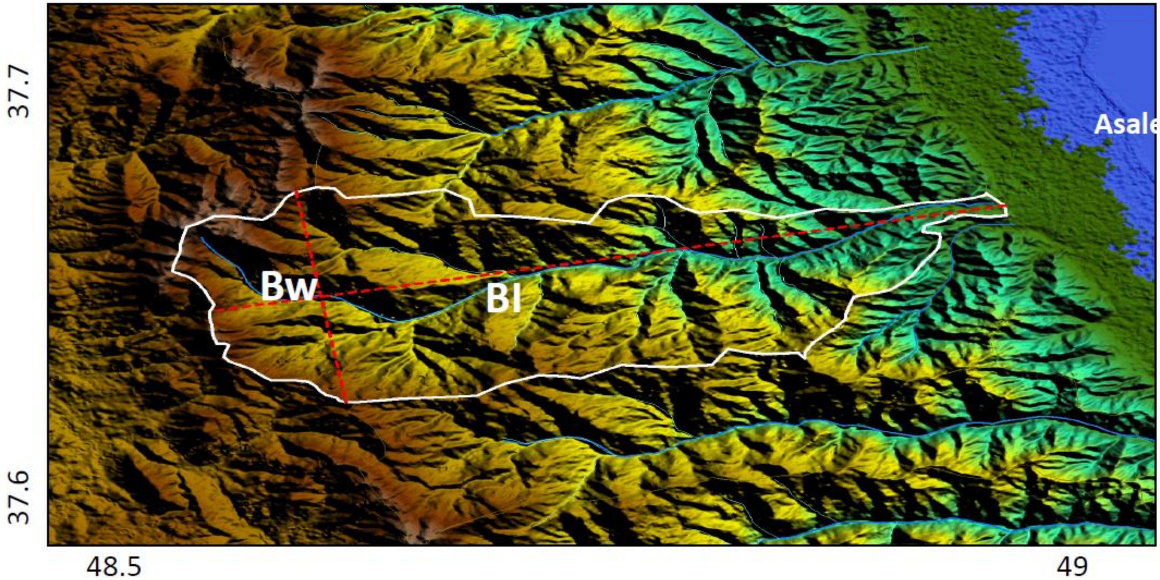

Figure 26: Display of Bs index in watershed number 20 in the field of digital elevation model (DEM30)

3-2-2 Drainage basin asymmetric factor (AF):

$AF=100(A_r/A_t)$

This index shows the lateral tilting of the basin compared to the main course of the river due to tectonic forces. Value of AF equal to 50, indicates no tilting and relatively stable conditions in the basin. If the index is less or more than 50, indicates the tilting of the basin, which can be caused by tectonic activities. (Figure *27* & Table *2*)

Table 2: Asymmetry index of the research area

Asymmetric Factor(AF)							
Basins	Ar(Km^2)	At(Km^2)	AF	Tilting part	Flow Direction of River	Tectonic Class	AF-50
17	7.82	15.17	51.54%	north	west to east	3	1.54
18	16.46	27.16	60.60%	north	west to east	2	10.6
19	281.25	587.82	47.84%	south	west to east	3	2.16
20	148	276.38	53.54%	north	west to east	3	3.54
21	28.84	53.42	53.98%	north	west to east	3	3.98
22	100.84	210.99	47.79%	south	west to east	3	2.21
23	123.45	259.52	47.56%	south	west to east	3	2.44
24	42.82	76.01	56.33%	north	west to east	3	6.33
AF Classification:|AF-50|<7 Low Activity,7<|AF-50|<15 Moderaite Activity,|AF-50|>15 High Activity							

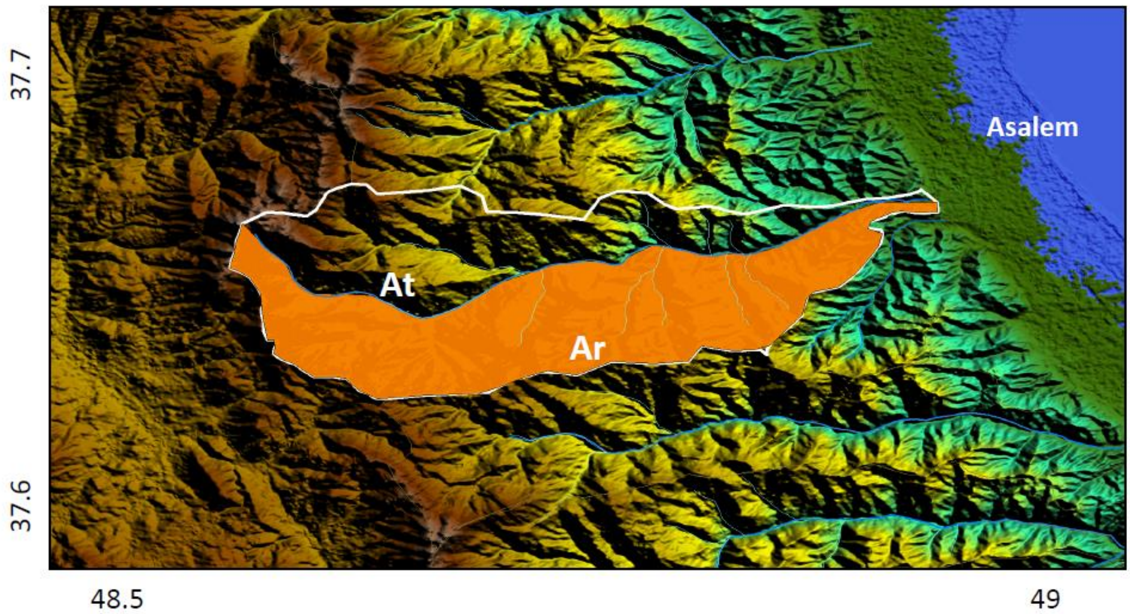

Figure 27: The AF index in basin number 20 with the background of the digital elevation model (DEM30)

3-2-3 Transverse topographic symmetry factor

$T=D_a/D_d$

This index can be considered as a quick method to detect the amount of tilting resulting from tectonic activity. Examining the number of changes in tilting in different parts of the same area reveals the difference in the amount of uplift. For a completely symmetrical basin, T=0. With the increase of asymmetry, the T index increases and finally approaches to 1. It is assumed that the dip of the layers has a negligible effect on the migration of the main river channel, therefore, the general migration is a reason for the tilting of the land. This analysis of the index is more suitable for drainage basins with a dendritic pattern. Values between 0.01-0.4 are tectonically active in category one, values between 0.05-0.09 are in category two, which are tectonically moderate. and values of 0.0-0.05 are placed in category three, which have little tectonic activity. (Figure *28* & Table *3*)

Table 3: Transverse topography asymmetry values of the studied area

Transverse Topographic symmetry Factor(T)				
Basins	Da	Dd	T	Tectonic Class
17	480	1339	0.358	1
18	501	1886	0.265	1
19	757	13794	0.054	2
20	1712	4981	0.343	1
21	226	2929	0.077	2
22	538	3965	0.135	1
23	2124	6143	0.345	1
24	700	1274	0.549	1
T classification:(0-0.05)Low Activity,(0.05-0.09)Moderate Activity,(0.1-0.4)High Activity				

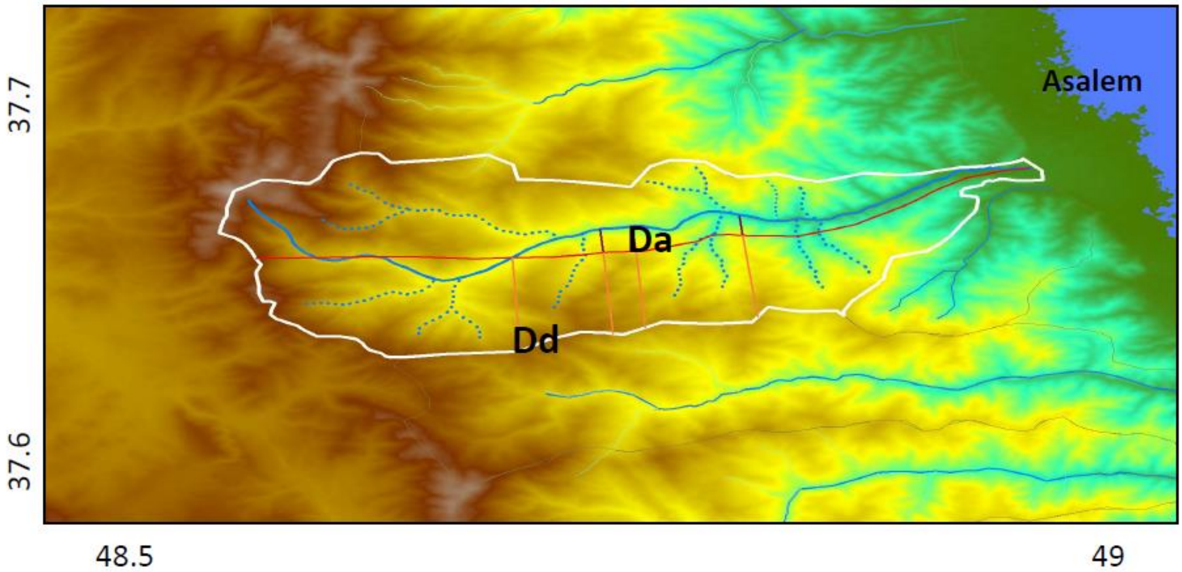

Figure 28: The T index in basin number 20 with background from digital elevation model (DEM30)

3-2-4 Ratio of Valley Floor width to Valley Height (V_f)

$V_f = 2Vf_w/[(E_{ld}-E_{sc}) + (E_{rd}-E_{sc})]$

The morphology of the valleys is one of the important indicators to determine the activity of tectonic forces in the region. V-shaped valleys have relatively high activity and those valleys with wide floors have less activity. This index indicates whether the river excavates its bed or whether it mainly erodes laterally. According to (Hamdouni et al) (2007) It can be concluded that V_f values less than (0.5) tectonically active, values (1-0.5) have moderate activity and more than (1) indicate basins with low tectonic activity. (Figure *29* & Table *4*)

Table 4: The index of the ratio of the width of the valley floor to the height of the valley

Ratio of Valley Floor to Valley Height						
Basins	Vfw (m)	Eid(m)	Erd(m)	Esc(m)	Vf	Tectonic Class
17	155	402	555	137	0.454	1
18	150	961	1415	150	0.21	1
19	168	613	482	168	0.41	1
20	199	962	899	199	0.289	1
21	82	543	486	82	0.342	1
22	80	721	721	80	0.172	1
23	90	753	750	90	0.19	1
24	100	1053	1382	358	0.116	1
Vf classification:(>1)Low Activity,(1-0.5)Moderate Activity,(<0.5)High Activity						

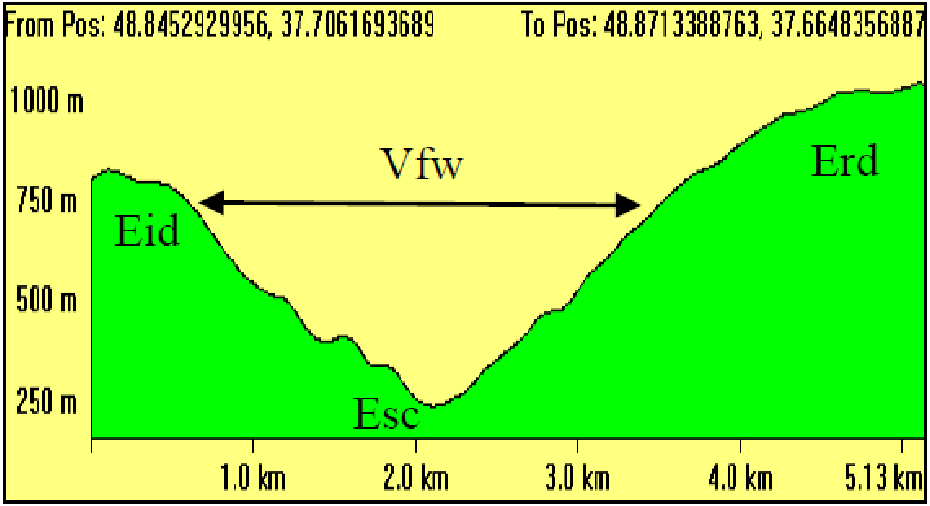
From Pos: 48.8452929956, 37.7061693689
To Pos: 48.8713388763, 37.6648356887
1000 m
750 m
500 m
250 m
Vfw
Eid
Erd
Esc
1.0 km
2.0 km
3.0 km
4.0 km
5.13 km

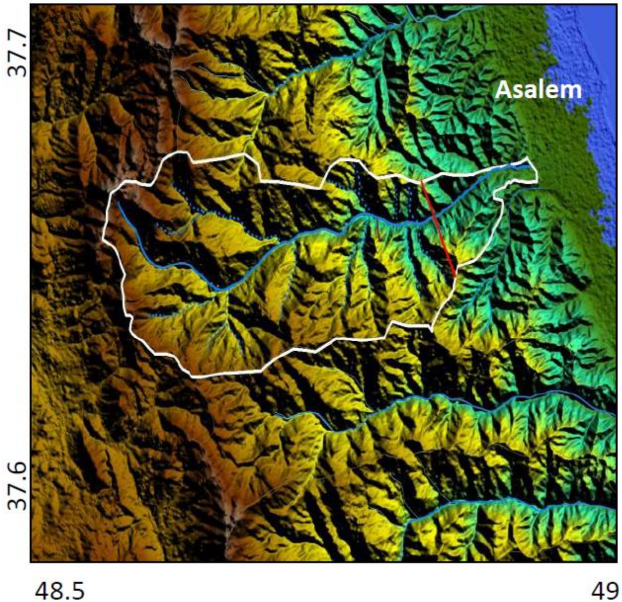

Figure 29: In the figure on the right, the red line shows the place of the profile in basin number 20 (on the background of the digital elevation model). The figure on the left shows the resultant profile.

3-2-5 Mountain Front Sinuosity index (S_{mf})

$S_{mf}=L_{mf}/L_s$

This index reflects the balance between climatic conditions, erosional forces, lithology and tectonic forces that tend to produce a straight mountain front coincident with an active range bounding fault. The mountain front in tectonically active areas is relatively straight and the amount of S_{mf} is low, if the amount of uplift is reduced, the erosional processes cause irregularity and sinousity of the mountain front, and the values of S_{mf} increases. Climate also has a significant effect on this index. In humid condition due to erosion, the mountain front lose its straight position and takes a sinous state, but in dry weather, the mountain front is less affected by erosion. (Figure *30* & Table *5*)

Table 5: The calculated mountain-front sinuosity index in the study area

<table>
<tr><th colspan="4">Mountain Front Sinuosity</th></tr>
<tr><th>Basin</th><th>ATF Segment</th><th>Smf</th><th>Tectonic Class</th></tr>
<tr><td>17</td><td rowspan="3">2</td><td rowspan="3">2.74</td><td rowspan="3">2</td></tr>
<tr><td>18</td></tr>
<tr><td>19</td></tr>
<tr><td>20</td><td rowspan="5">3</td><td rowspan="5">2.05</td><td rowspan="5">2</td></tr>
<tr><td>21</td></tr>
<tr><td>22</td></tr>
<tr><td>23</td></tr>
<tr><td>24</td></tr>
<tr><td colspan="4">Smf Classification:(2.8-3.5)Low Activity,(1.8-2.3)Moderate Activity,(<1.53)High Activity</td></tr>
</table>

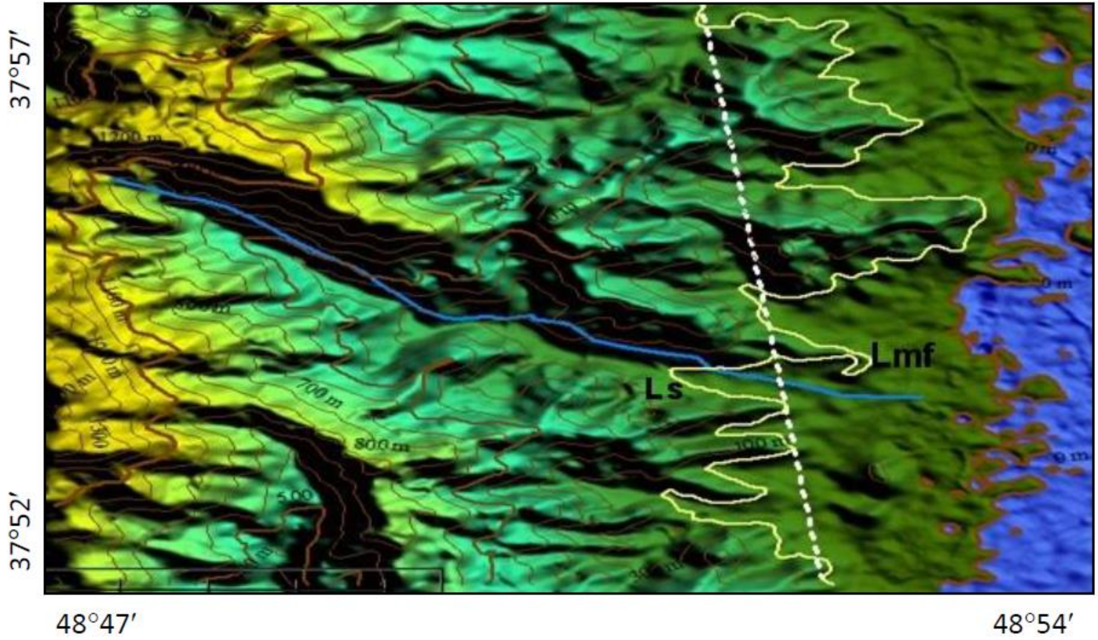

Figure 30: How to measure L_{mf} and L_s to calculate Smf on Talash ranges using DEM30

3-2-6 Hypsometry

Minimum height - maximum height / minimum height - average height = hypsometric integral

Hypsometry is an index that shows the distribution of height in a specific area. This index is usually calculated for a specific drainage basin and is independent of its area. The necessary data to calculate the integral of hypsometry is obtained from the digital elevation model of the area. The value of this index is equal to the area under the surface of the hypsometric curve. The high values of this index indicate the active and young areas, and the low values are related to the old areas that are dominated by the erosion process and are less affected by the active tectonics of the region (Hamdouni et al., 2007). Values greater than 0.5 indicate high tectonic activity, values around 0.5 indicate moderate tectonic activity, and values less than 0.5 indicate low tectonic activity. (Keller & Pinter, 2002). (Table *6*)

Table 6: Hypsometric index calculated in the studied area

Hypsometric Integral					
Basins	Hmax(m)	Hmin(m)	Hmean(m)	H.I.	Tectonic Class
17	1300	60	522	0.372	3
18	1627	34	511	0.299	3
19	3227	42	1173	0.355	3
20	2991	86	1267	0.406	2
21	1600	15	501	0.306	3
22	2870	78	1097	0.364	3
23	2889	52	1027	0.3436	3
24	1840	209	902	0.424	2
Hi Classification:(<0.5)Low Activity,(0.5)Moderate Activity,(>0.5)High Activity					

3-2-7- Basin 17

This basin is located in the west of Lisar city, with an area of about 16.25 square kilometers (Figure *31*). This basin is fed by one of the branches of the Lisar river. The B_s index of the basin is calculated around 1.581, and it is placed in tectonic class 3. It is worth mentioning, that value 1 is in the active range, tectonic class 2 is in the moderate tectonic activity, and value 3 is in the category of low activity. The valley width to depth (V_f) indexof the basin is 0.454, which will be placed in tectonic class 1.

The asymmetry index of the basin (AF) is calculated as 51.54%, which places the basin in tectonic class 3. The valu hypsometry of is 0.372, which will be in category 3. Transverse topography factor (T) 0.358 was calculated, which is placed in tectonic class 1.

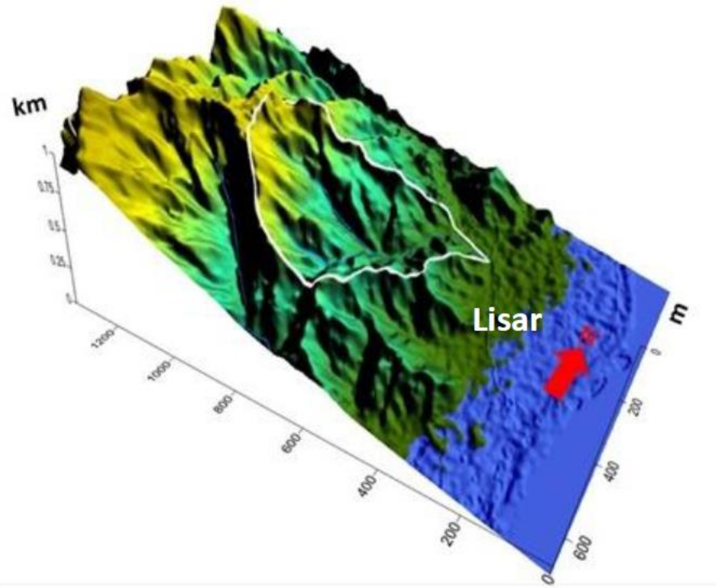

Figure 31: 3-D view of basin 17 with the background of digital elevation model (DEM30)

3-2-8- Basin 18

This basin with an area of 25.86 square kilometers, is fed by an independent river, which at the end of this basin reaches Jokandan region (Figure *32*). The value of B_s of the drainage basin measured as 1.94 and it is placed in tectonic category 3. The V_f index value is 0.21 and it is placed in tectonic class 1. The A_f index is calculated to be 60.6% and it is placed in category 1. The hypsometry of this basin is 0.299, which is belongs to the old basins in class 3, and the transverse topography factor was measured at 0.265 and it is placed in class 1.

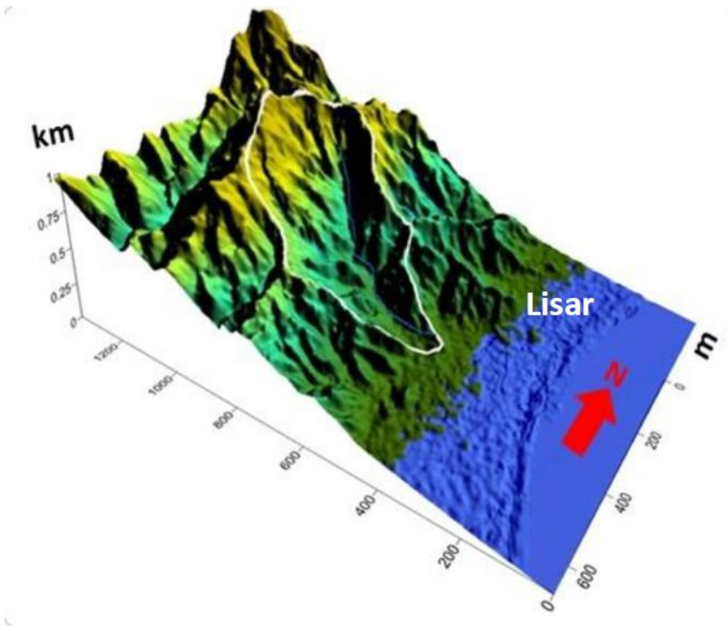

Figure 32: 3-D view of basin 18 with the background of digital elevation model (DEM30)

3-2-9- Basin 19

This basin with an area of about 580.6 square kilometers is one of the largest basins in studied area, and is fed by, Aq Oler, Vasnesar and Ler Rivers (Figure

33) of Hashtpar. The indices calculated in this basin are as follows. The shape index of the drainage basin is 1.16, which is in tectonic class 3. The asymmetry of the catchment basin is 47.84%, which is included in tectonic class 3, the hypsometry of this basin was measured as 0.355, which is in the range of tectonic class 3, and finally, the transverse topography factor was obtained as 0.054, which is Rank 2.

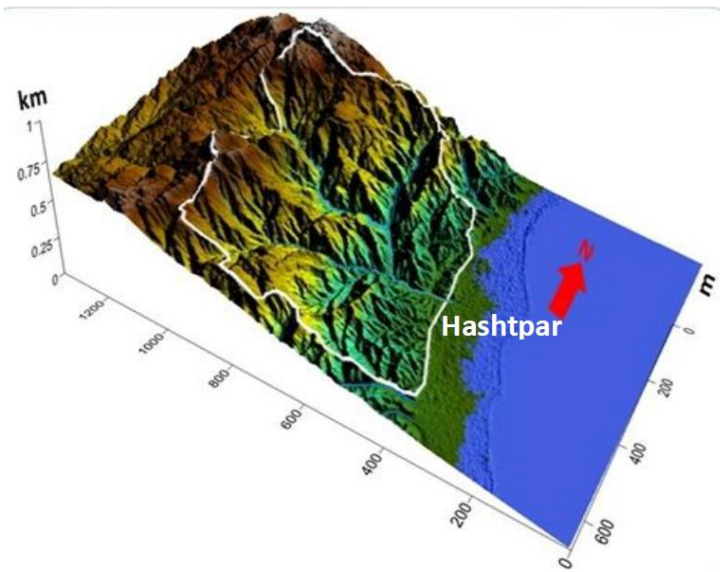

Figure 33: 3-D view of basin 19 with the background of digital elevation model (DEM30)

3-2-10- Basin 20

This basin with an area of about 260.5 square kilometers, is fed by the Bize Si River, which originates from Sultan Khoni Mountains (Figure *34*). This basin is located in the vicinity of Asalem city. The B_s index of the basin 2.22 that is in the 3rd tectonic category, the index of V_f value was as 0.289 and it is placed in the tectonic class 1, the asymmetry index of the catchment basin is 53.54%, which is in the 3rd tectonic category. The hypsometry of this basin is 0.406 and is placed in tectonic class 2, and the transverse topography factor is calculated as 0.343, which is placed in tectonic class 1.

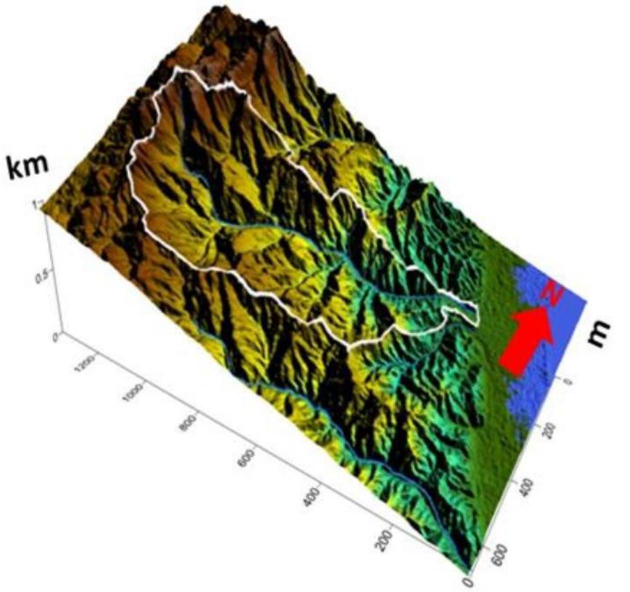

Figure 34: 3D view of basin 20 with the background of digital elevation model (DEM30)

3-2-11- Basin 21

This basin with an area of about 40.41 square kilometers leads to Khalaf Abad region (Figure 35). The morphometric indices of the basin are as follows: the shape of the drainage basin is 1.358 and it is placed in tectonic category 3. The width of the valley floor to the depth is 0.342 and its tectonic class is 1, the asymmetry of the catchment basin is 53.98%, for which category 3 is considered. and finally, the transverse topography factor is 0.077 and it is in tectonic class 2.

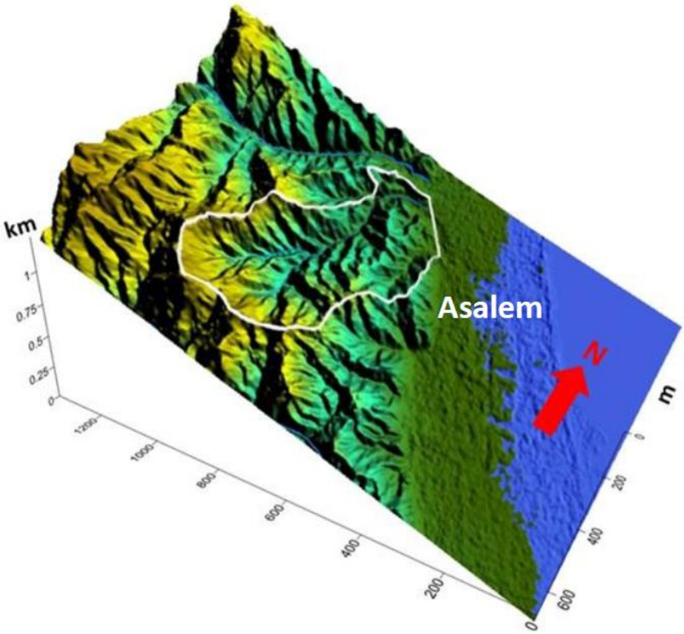

Figure 35: 3D view of basin 21 with the background of digital elevation model (DEM30)

3-2-12- Basin 22

This basin has an area of 207.1 square kilometers and is fed by the Lumber River, and this basin ends in the village of Molimeleh (Figure 36). The shape index of the measured drainage basin is 3.92, which is in tectonic class 2. The valley width to depent index is 0.172 and it will be placed in tectonic category 1. The asymmetry index of the catchment basin is calculated at about 47.79% and its tectonic category is 3. The hypsometric curve of this basin is 0.364 which shows tectonic class 3. The transverse topography factor is 0.135 and its tectonic category is 1.

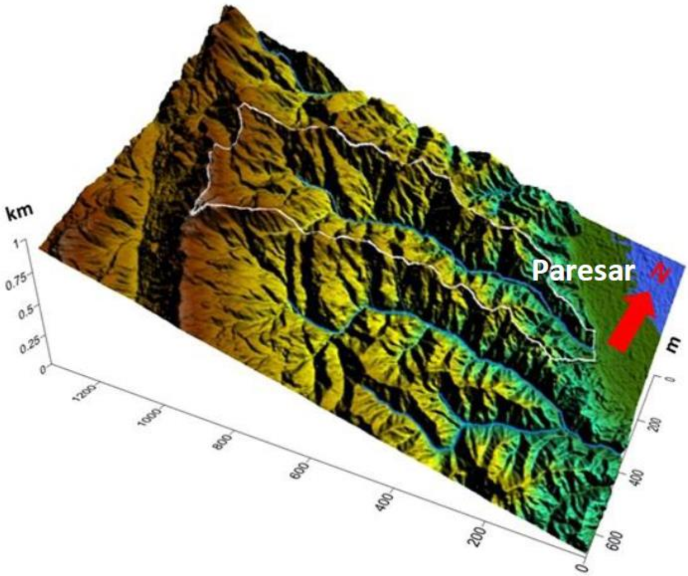

Figure 36: 3D view of basin 22 with the background of digital elevation model (DEM30)

3-2-13- Basin 23

This basin is fed by the Shafarood River, which originates from the Tiref Mountains. This river passes through Rezvanshahr and flows into the Caspian (Figure *37*). The area of this basin is estimated at 263.4 square kilometers. The shape index of the drainage basin is 2.56, which is in tectonic class 3. The valley width to depth index is 0.19, which will be in tectonic class 1. The asymmetry index of the drainage basin is 47.56%, and its tectonic category is 3. The hypsometry curve of the basin was measured as 0.343 and the transverse topography factor as 0.345, which will be placed in tectonic category 3 and 1, respectively.

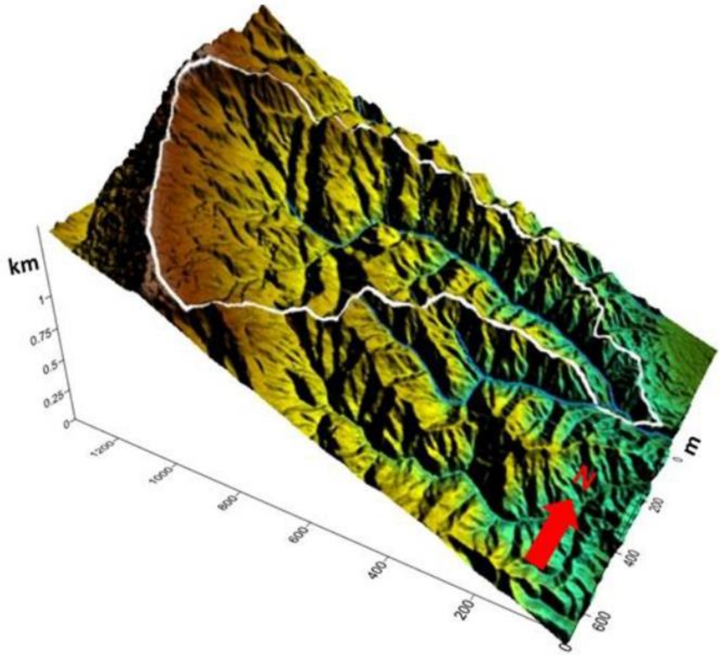

Figure 37: 3D view of basin 23 with the background of digital elevation model (DEM30)

3-2-14- Basin 24

This basin estimated at 82.75 square kilometers (Figure *38*). The shape index of the drainage basin is 2.409, which is in tectonic class 3, the valley floor width to depth index is 0.116 and is in the tectonic category 1. The asymmetry index of the drainage basin was measured at 56.33% and it is placed in class 1. The hypsometry of this basin is 0.424 and it is placed in tectonic category 2, and the transverse topography factor is 0.549 and will be ranked 1.

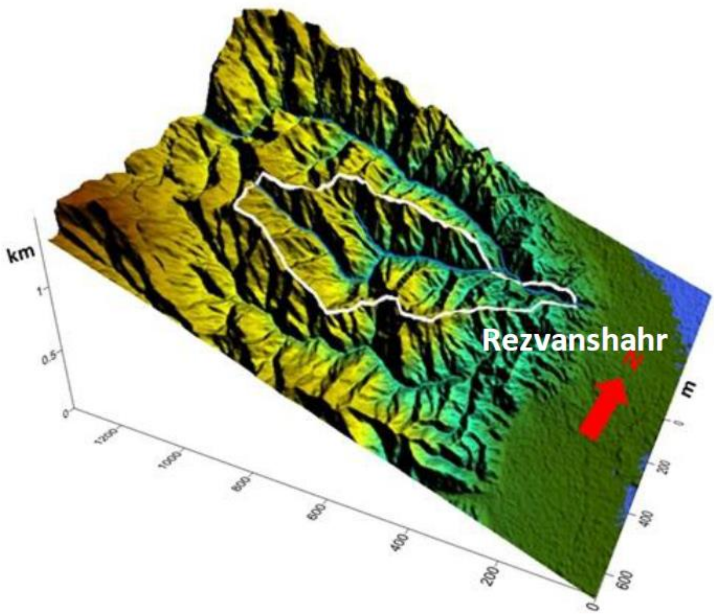

Figure 38: 3D view of basin 24 with the background of digital elevation model (DEM30)

3-3 Investigation of horizontal and vertical displacements in the studied area

In this part of the research, the features that have been displaced along the Astara fault will be examined. According to the Kaveh et.al, Astara fault system consist of two thrust and right lateral strike-slip components. The thrust component consists of three segment and the right-slip fault consist of two segments. In each part of the fault, length of the profile, azimuth the coordinates of the starting and ending point of the profile, and the horizontal and vertical displacements are calculated (Figure *39*). Horizontal displacements (H) with an approximate error of ±30 meters and vertical displacements with an error of ±5 meters have been measured. The tectonic classification of displacements is as follows: displacements less than 200 meters in the A, displacement of 200-400 meters in category B, displacement of 400-600 meters in category C, displacement of 600-800 meters in category D, more than 800 meters will be placed in category E.

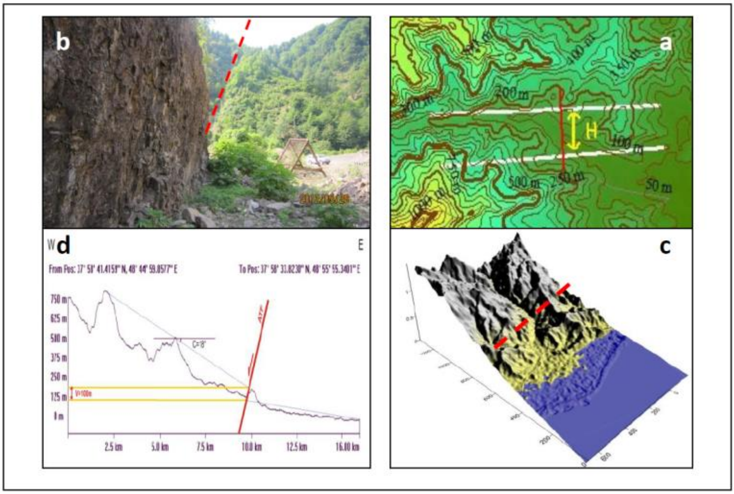

Figure 39: a) Calculation of horizontal displacement on a DEM30 background. b) The dashed line where the fault trace. C) 3-D plan from the rightlateral movement of the river due to fault activity in the Global mapper software (dashed line show the fault trace). d) Combination of two elevated section Corel software.

3-4 Astara fault morphotectonics

3-4-1 Morphological evidences

In order to measure the amount of deformation caused by tectonic processes, it is necessary to have features that have been displaced due to the movement of the fault (Burbank & Anderson, 2001). In order to measure the amount of displacement, the present displaced feature must be carefully returned to the state before the displacement (Burbank &Anderson,2001).

The best identified geomorphological markers are landscapes, levels, or linear trends that have three important features: 1) the ability to identify geometry before deformation 2) age determination 3) high persistence potential in the geological time scale. Some of the important evidences are as follows:

3-4-1-1 Shutter ridges:

A ridge offset by a strike-slip fault such that the fault is Juxtaposed against the gully ridge above the fault (Figure *40*).

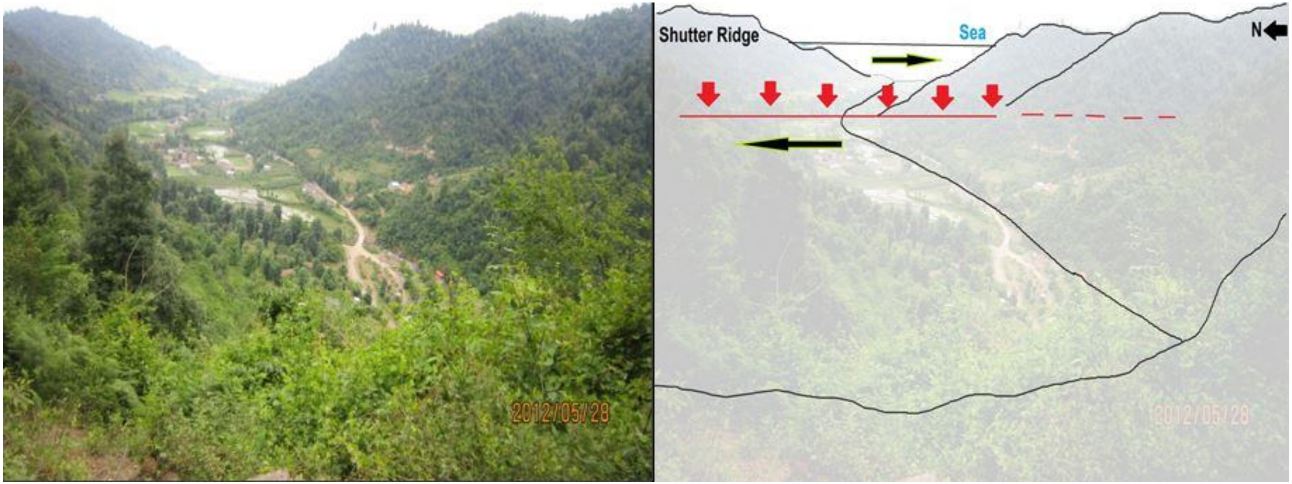

Figure 40: The view of a ridge that has caused the river to displace due to the right-lateral movement. The view is to the east in the village of Havigh with the coordinates N38°17′54.5″and E48°49′1.1″.

3-4-1-2- Scarp

A slope steeper than the surrounding topography; related to a change in material, process, or geometry history (Figure *41*).

Figure 41: The scarp observed with almost 2 meters height in the beginning of Gisum road. The location of the photo on the left is near the village of Gisum, 5 kilometers south of Asalem.

3-4-1-3 Deflected Streams

A stream that follows a strike-slip fault along some or all of its length (Figure *42*).

Figure 42: Right lateral river displacement by Astara fault, looking south. The exact location of this displacement (is in the Lisar Valley with coordinates N37°58′38.8″ and E48°51′54.1″).

3-4-1-4 Offset Streams

A stream the channel of which is displaced across a Strike-slip fault.

3-5 Subsurface Data

3-5-1 Review of GPR data

About forty-five profiles have been collected by the geophysics group of the Geological survey of Iran, of which four profiles are located in the studied area and used for subsurface investigation. The information of this section was compiled by Mohammadi Vizheh (2013) (Figure *43*).

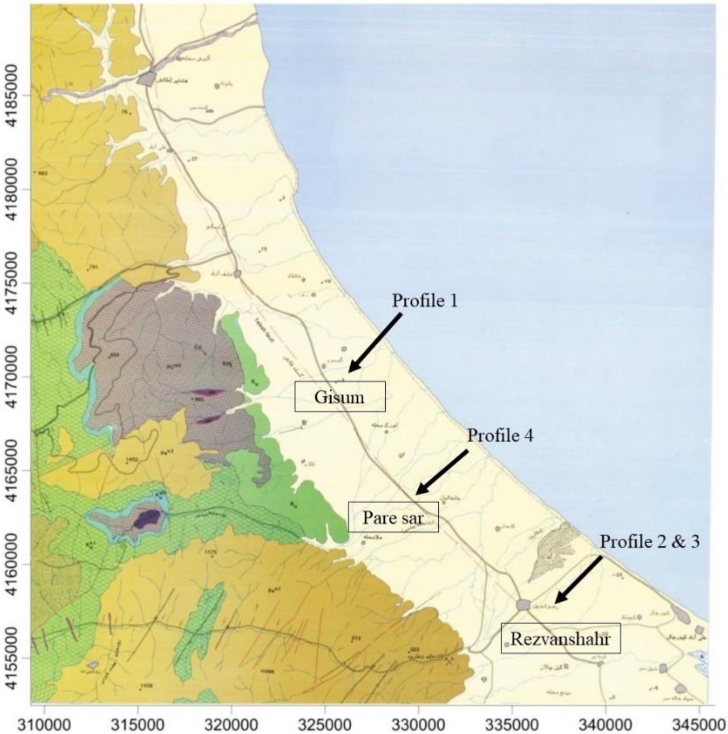

Figure 43: Location of profiles 1 to 4 in GPR studies. (Khalkhal-Rezvanshahr sheet).

3-5-1-1 Profile 1

This 3890-meter-long profile was surveyd along the Gisum road (Figure *44*). In the processed section of this profile, there are two anomalous areas. In Figure *45* the depth section of the first anomaly and in Figure *46* the depth section of the second anomaly toghether with the topography of this part of the profile are shown.

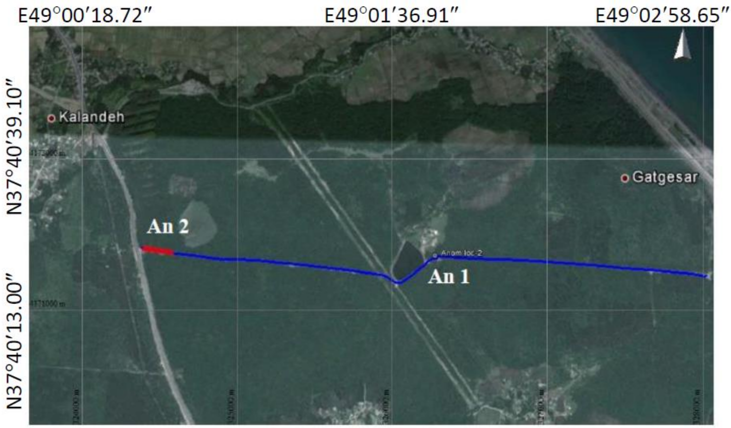

Figure 44: Satellite image of the surveyed area of Profile 1 (Mohammadi Vizheh, 2013).

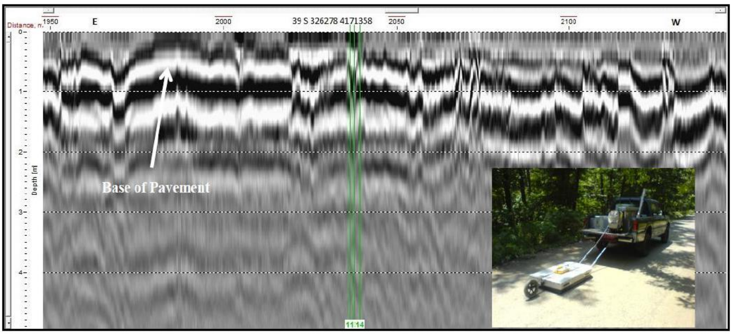

Figure 45: Depth section of the first anomaly area along profile 1, using a 100 MHz cover antenna (Mohammadi Vizheh, 2013).

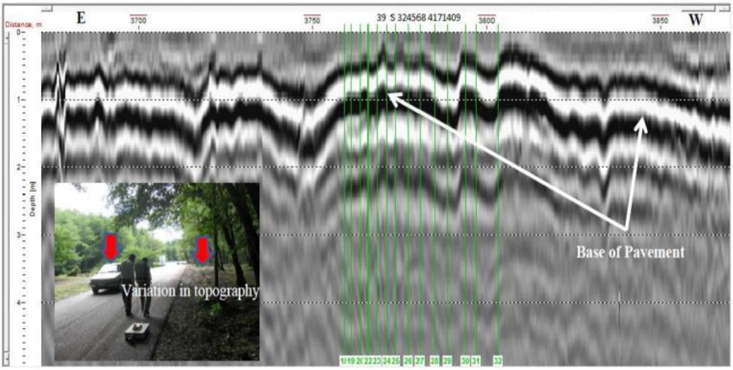

Figure 46: Depth section of the second anomalous area along profile 1 using a 100 MHz cover antenna (Mohammadi Vizheh, 2013).

Along profile 1, a displacement of about 2 meters can be seen. This rough topography in the recent sediments can be caused by young tectonic movements due to the activity of the Astara fault or its branches in this area (Figure *47*).

Figure 47: A part of profile 1 which is shown with a red line on a background of Google Earth satellite images (Mohammadi Vizheh, 2013).

3-5-1-2- Profiles 2 and 3

Profile 2 using a 100 MHz antenna with a length of 6360 meters surveyed along Tazeh Abad road approximately in an east-west. Also, profile 3 using a 100 MHz antenna with a length of 7836 meters surveyed along Punel-Razvanshahr road in southwest-northeast direction. Most of the anomalous feature along these profiles can be seen in urban facilities, including canals, pipes, and buried cables.

3-5-1-3- Profile 4

This profile was surveyed with a long of 3278 meters, along the ParehSar power plant in a northwest-southeast trend. In this profile, like profile 1, two abnormal areas can be recognized. These areas can be recognized at the distances of 1950 meters and 2200 meters of the profile. Due to some problems more detailed investigation and field visit of these areas it is necessary to confirm or rejecting of the tectonic activity. The depth of penetration in this area is not significant as in profile 1. This is due to the high electrical conductivity of the subsurface soils in this area. The presence of clay sediments and significant soil moisture has caused the information to be limited to the upper layers (Figure *48* & Figure *49* & Figure *50*).

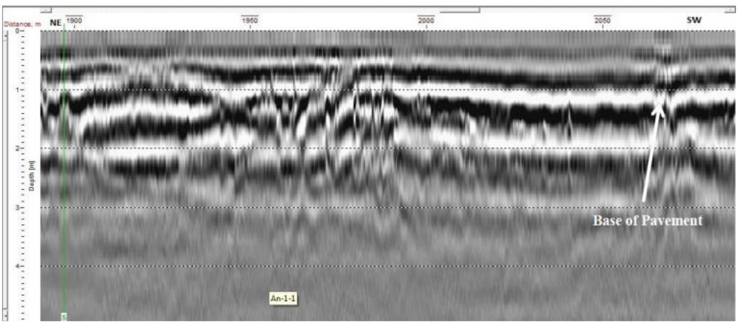

Figure 48: Depth section of the first anomalous area on profile 4 using a 100 MHz cover antenna (Mohammadi Vizheh, 2013).

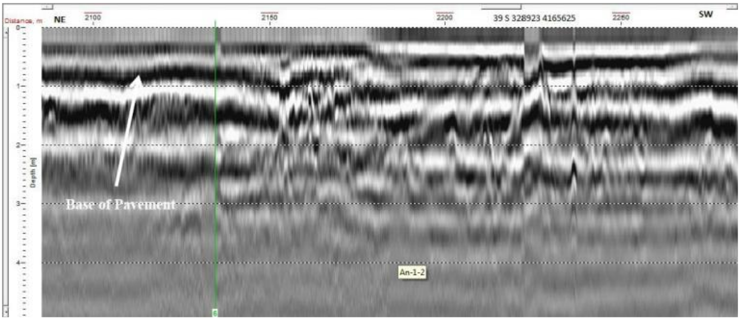

Figure 49: Depth section of the second anomalous area on profile 4 using a 100 MHz cover antenna (Mohammadi Vizheh, 2013).

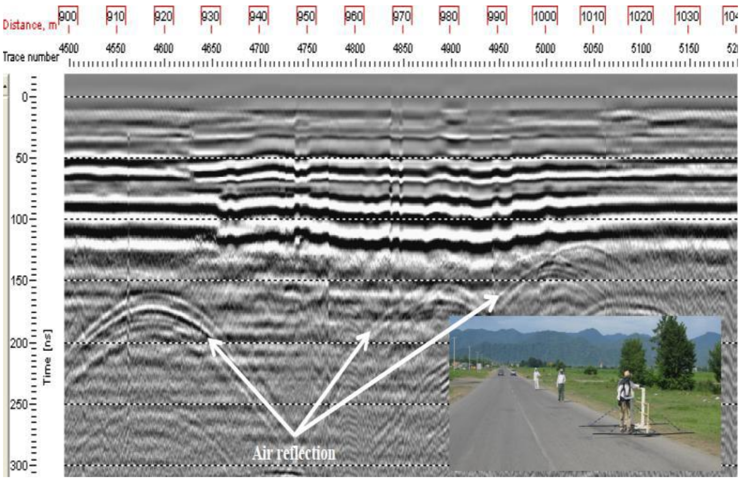

Figure 50: Time section of a part of profile 4 using a 25 MHz antenna. The hyperbolas area response to the beams and masts, which are marked with white arrows. (Mohammadi Vizheh, 2013).

3-5-2 Analysis of the results of resistivity method

On each profile, three different resistivity arrays, including Dipole-Dipole, Wenner and Pole-Dipole carried out, and the results of all three arrangements will be evaluated in this section (Figure *51*).

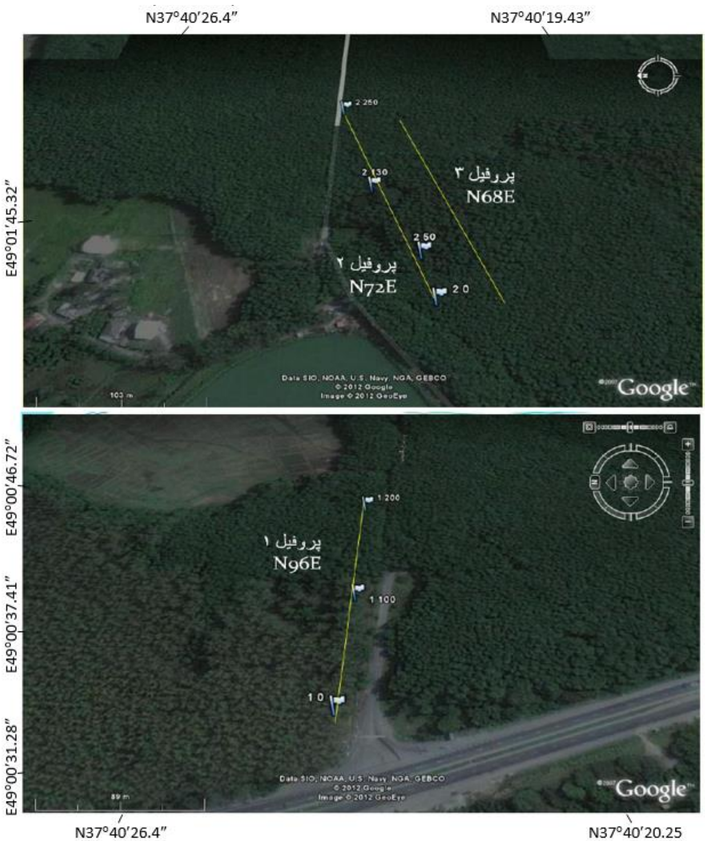

Figure 51: Location and position of profiles 1 to 3 using Google Earth. View from west to east in the beginning of Gisum beach road.

3-5-2-1 Analysis the results of three arrays surveyed along profile 1

Figure *52* shows the results of three sections carried out on profile one along with the GPR section. Due to the wetness and consequently the low electrical resistivity on the surface, the depth of penetration is very low (about two meters), and apart from the surface variation, not much information about the depth and discontinuities is obtained in GPR surveying. The anomalies obtained in the three modeled sections, especially between stations 70 and 140 in the resistant layer, are in good agreement with each other in the surface and depth. Of course, in the Wenner array, due to the short electrode distance, more details of the anomalies can be seen, but the depth of investigation is low, but instead, the anomalies have less details in the pole-bipole section, and in some areas, the shape of the anomaly with other two sections is slightly different so that the resistant anomaly, which is located at a depth of 15 meters between stations 70 and 140, can be seen continuously in this section, but depth of the observed discontinuity in the other two sections between stations 100 and 120, is more than other arrays.

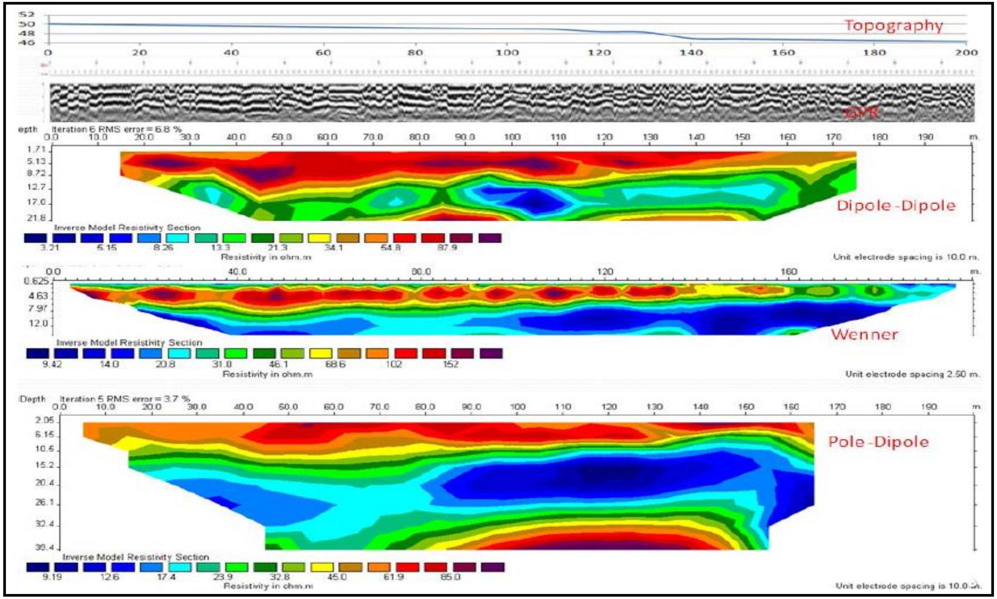

Figure 52: Resistivity modeling cross-sections with three different arrays along with the GPR cross-section on profile one, which shows the results obtained from the dipole-dipole, Wenner and pole-dipole arrays from top to bottom resistivity (Razavi, 2013).

3-5-2-2 Analysis of the results of surveyed sections along profile 2

The results of minimum and maximum values of dipole-dipole resistivity with 2 meters station interval along the Profile are 13.6 and 104 Ohmmeters respectively (Figure *53*). The minimum and maximum values of the same surveying with 10m station interval are 15.3 and 49.7 Ohmmeters respectively (Figure 54) Figure 55, Show the modeled map of resistivity with topography correction. A total of 422 stations have been measured by resistivity method

In Figure *53*, the same sequence of layers with high and low resistivity that can be seen in profile 1 can also be seen in this section. Due to distorsion of layers, beneath stations 120 to 150 the possibility of the faults in this area is expectative. Faults are shown on the map with dashed lines (Figure *54* & Figure *55*).

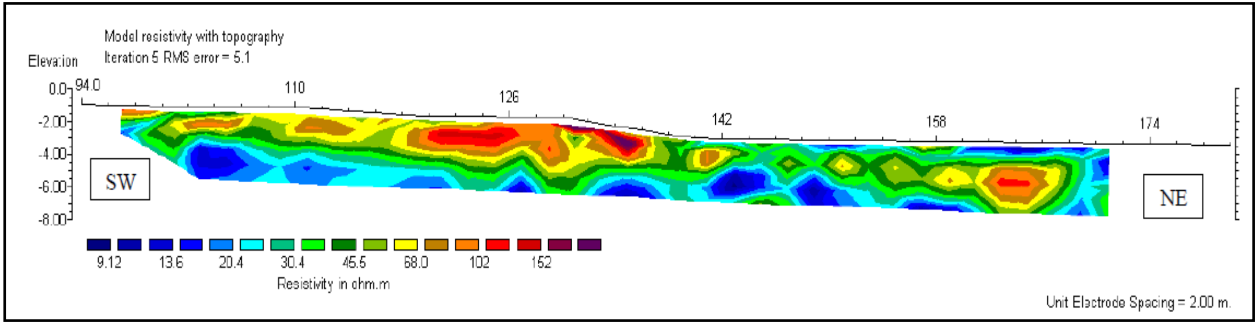

Figure 53: Resistivity modeling cross-section by applying topography correction (with 2 m station intervals) (Razavi, 2013).

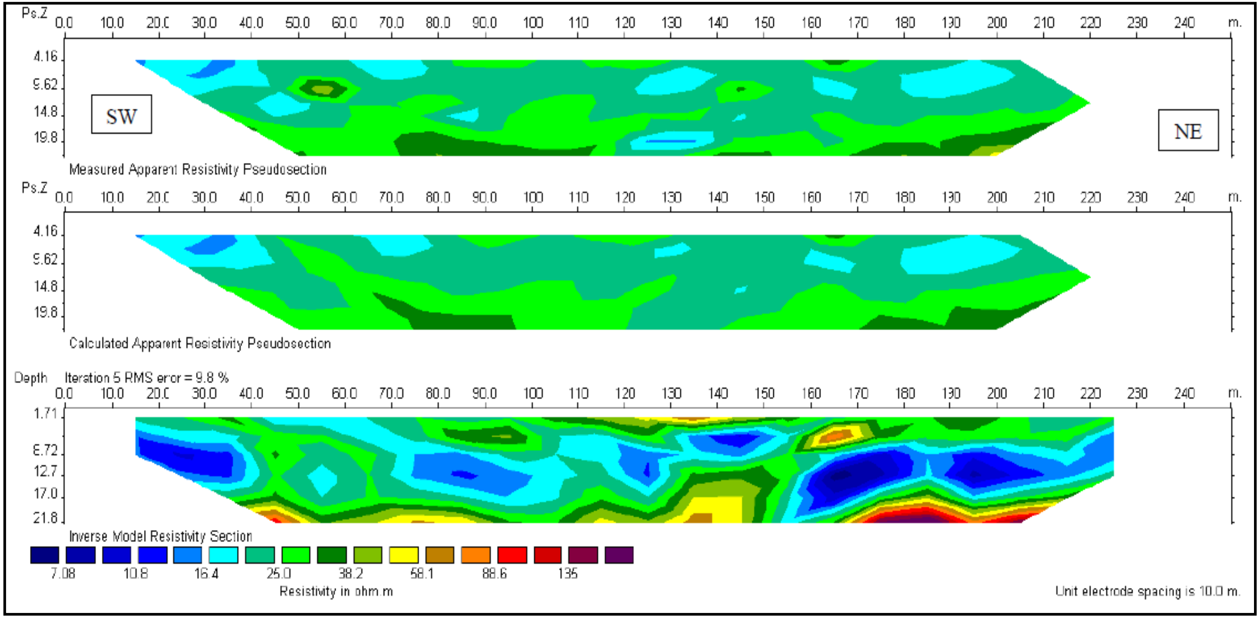

Figure 54: Resistivity pseudo-sections along with the model (with 10-meter station intervals) (Razavi, 2012).

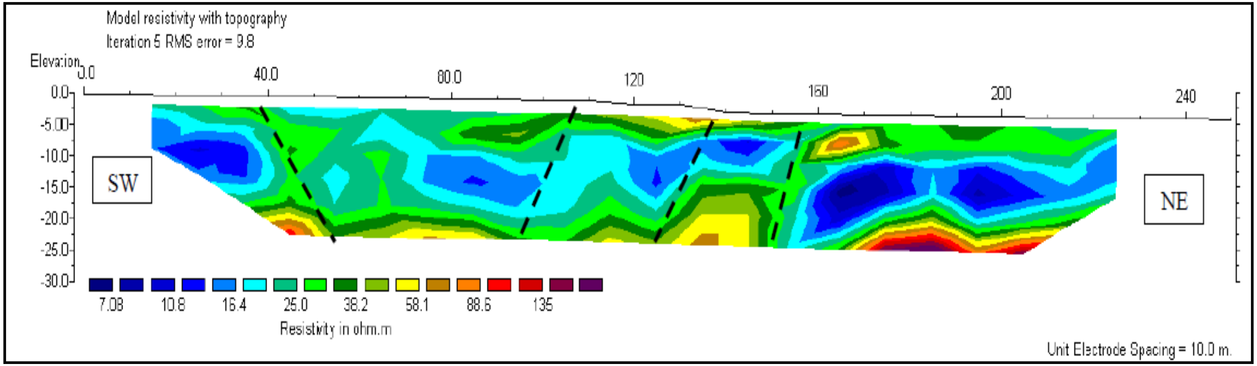

Figure 55: Resistivity modeling cross-section with topography correction (probable faults are marked with black dashed lines) (Razavi, 2013).

3-5-2-3 Analysis the results of surveyed section along profile 3

This section was surveyed with a station distance of 10 meters using dipole-dipole array. The lowest and highest numerical value of the resistivity is 15.5- and 50.6-ohm meters, respectively, and a total of 126 station has been measured by the resistivity method. In this profile, the thickness of the surface resistant layer (indigo to green color spectrum) and its resistivity has been greatly reduced. The wet layer is close to the surface and is located at a depth of 5 to 12 meters. The resistant layer that was present in the depth in the previous profile, in this profile, it is close to the surface and has reached a depth of 12 meters. This layer show two discontinuities under the 130. to 140 and 100 to 110 stations. Discontinuities between station 100 to 150 may be due to the fault activity, and shown by a dashed line.

By comparing profiles two and three, it is clear that the shapes of the anomalies are similar to each other and there is only a difference in the thickness of the layers and their depth (Figure *56* & Figure *57*).

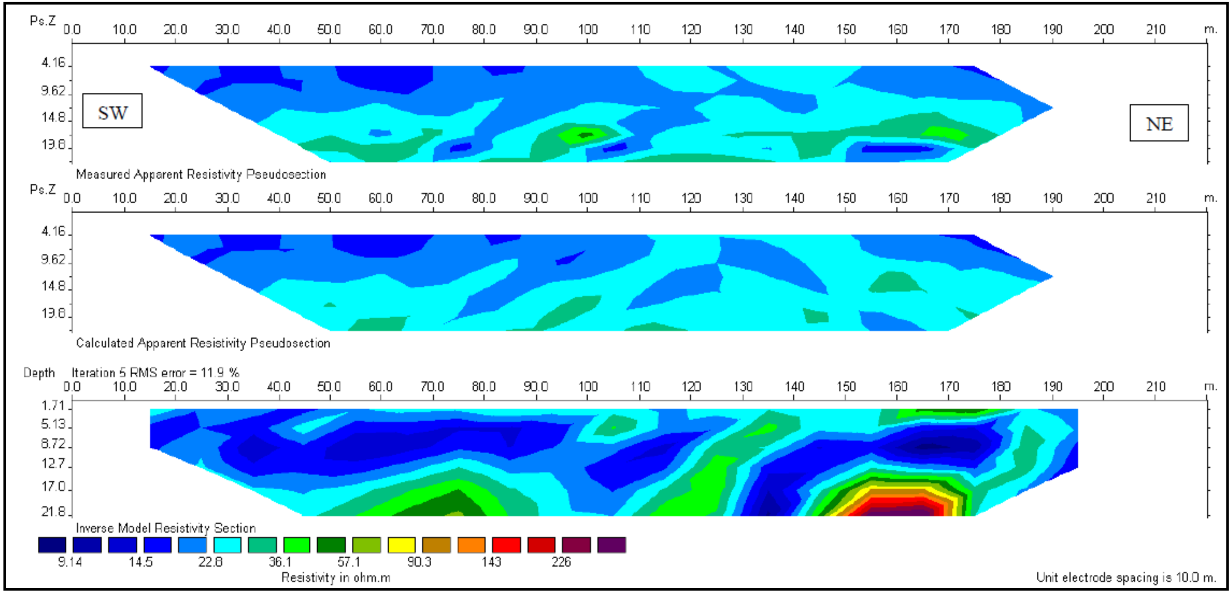

Figure 56: Resistivity pseudo-sections with model, profile three (Razavi, 2013).

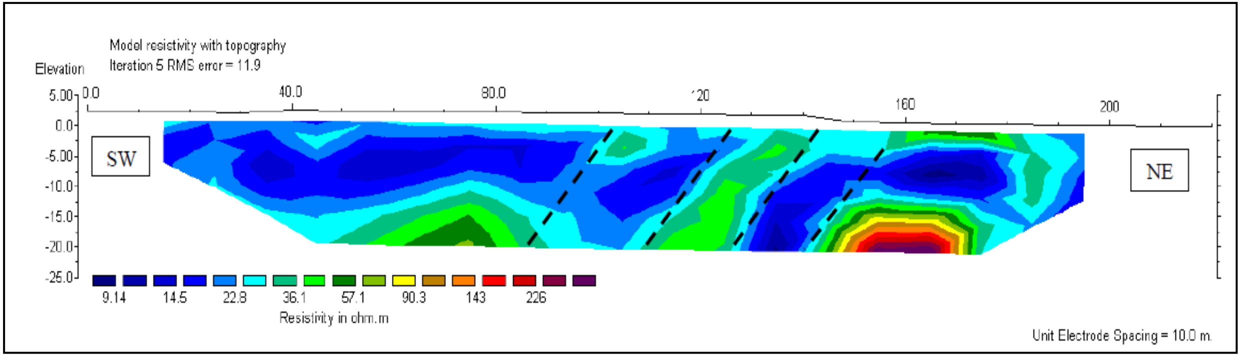

Figure 57: Sections of resistivity modeling by applying topography correction on profile three (inferred faults are marked with black dashed lines) (Razavi, 2013).

3-5-3 Review of geomagnetic data

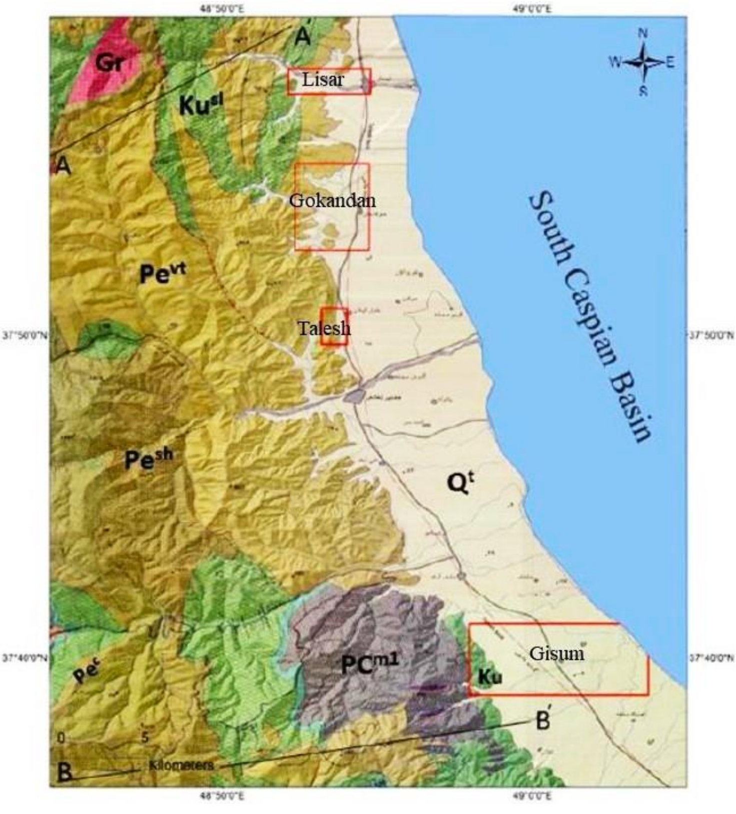

Figure 58: The geological map of the area on the digital elevation model. Boxes show the places studied by magnetic method. DEM (http://asterweb.jpl.nasa.gov/gdem-wist.asp)

3-5-3-1 Gisum

In order to detect the trace of the Astara fault, three surveys have been carried out in the Gisum area (Figure 59). The magnetic survey covers the entire area from the sea coast to the slopes of Talash mountains (about 7.5 km wide). A small part of the studied area is covered with reef and sandy limestone with Upper Cretaceous age, and the rest of the survey area is covered with Quaternary alluvial sediments.

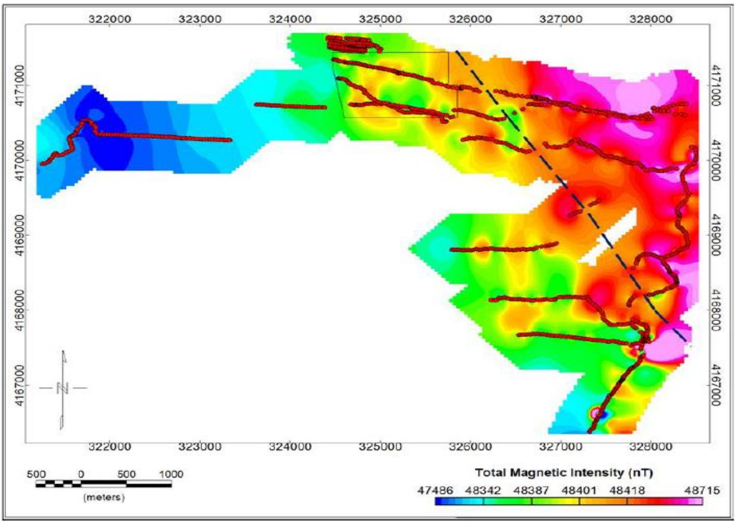

Figure 59: The total magnetic field intensity map in the first stage surveying of Gisum region. The dashed line shows the location of the high voltage power line (Asadi, 2013).

The distance between surveyed points is 30 meters and the distance between surveyed lines is 500 meters, and the number of measured points is 1,436.

In the second phase of the survey, the surveying was carried out in an area with a smaller area and in accordance with one of the linear trends observed in the magnetic map of the first phase of the survey. The trend of the lines is east-west and parallel to each other. The number of survey points are 1602 and the number of survey lines are 23. The result of the total magnetic field is shown on Figure *60*. The dark blue color indicates the minimum field intensity, the pink color indicates the maximum field intensity. The maximum value of the field is 48462 nano tesla and the minimum value is 48381 nano Tesla. There are three parallel linear magnetic anomalies with northwest-southeast trend.

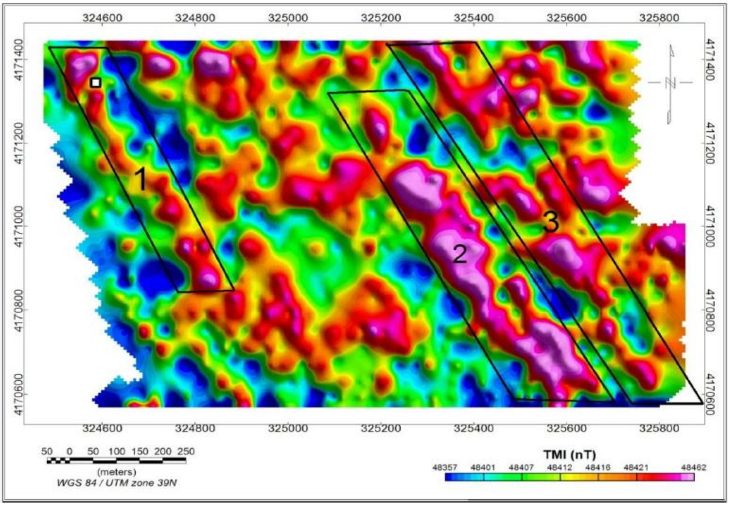

Figure 60: The map of the total magnetic field. Three linear mentioned trends are shown in the Box. The small white square is the sign of the spring (Asadi, 2013).

In the third stage of surveying, in order to determine whether the continuation of linear trends can be seen in other parts of the area, data surveying continued to the south of the network. Due to the proximity to the village of Gisum, it was not possible to carry out magnetic survey towards the southern border of the previous network. The distance of the station are 20 meters and the distance of surveyed lines are 40 meters. The direction of surveyed lines is east-west. The number of stations is 276, the number of surveyed lines is 8. The maximum value of anomaly is 171 nanotesla and the minimum is 94 nanotesla, the difference between the maximum and minimum is 77 nanotesla. Only a linear trend can be seen in this map.

Total horizontal and vertical derivatives filters show well the edges of anomalous sources, but acceptable solutions for the analytical signal were not obtained. This is probably due to the high depth of the anomaly source compared to its thickness. The good response of the magnetic field to the vertical and horizontal derivative and short wavelength of the observed magnetic linear trends also indicate the low depth of the magnetic sources. Since the application of different filters to identify the edge and center of the sources has almost the same answers, it can be concluded that the width of the source is narrow. Using the same filter, two other linear trends were also revealed, which seem to originate from the same source.

To estimate the depth of the main linear trend, Euler's deconvolution method was used. The answers were analyzed with the value of the structure index and different windows. With each value of the structure index and the size of the window, the answers are obtained linearly with the trend of lines. The obtained answers were very close to each other and at first glance, it is not possible to choose the best answer for the structure index and window size based on the standard deviation of the answers. Considering the density of the answers and the change in the obtained depths, the best answer for the structure index is 0.5 for a depth of 15 to 22 meters.

Perpendicular to the linear trends, 8 resistivity and induced polarization profiles carried out in three different locations. In 4 profiles, resistivity anomalies are accordant to the location of magnetic anomalies. In Pseudo-sections 1 and 2, resistance anomalies it does not show significant electrical resistivity. In Pseudo-section 3, there are two areas with higher electrical resistivity values, which cannot be interpreted due to their location in the lower part of the map and the possibility of modeling errors. In pseudo-section 4, two areas with lower resistivity are seen, which is equal to the electrical resistivity of the lower part of the map to a depth of 19 meters. In maps 7 and 8, the pole-dipole method shows almost the same answer. An area with a width of about 20 meters, can be followed in depth from 18 meters. The area with low electrical resistivity from the surface to a depth of 18 meters is related to the flow of underground water and water saturated layers. The induced polarization method also shows the existence of an area with higher chargeability, which is consistent with the answer obtained from the resistivity method. The high resistivity of the deeper layers can be the result of the sedimentary layers of sand and gravel.

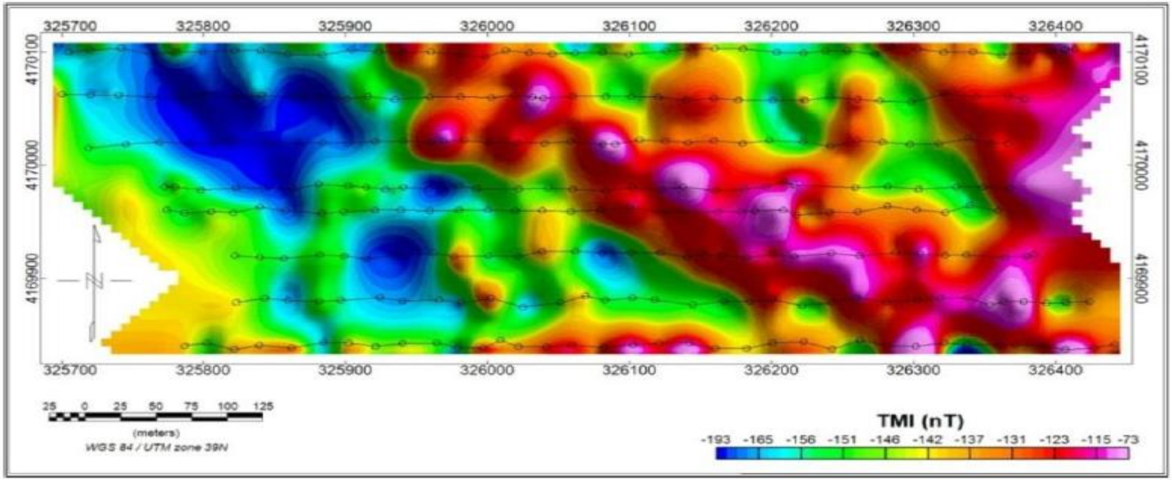

Figure 61: Magnetic field anomaly map after removing the geomagnetic field component (Asadi, 2013).

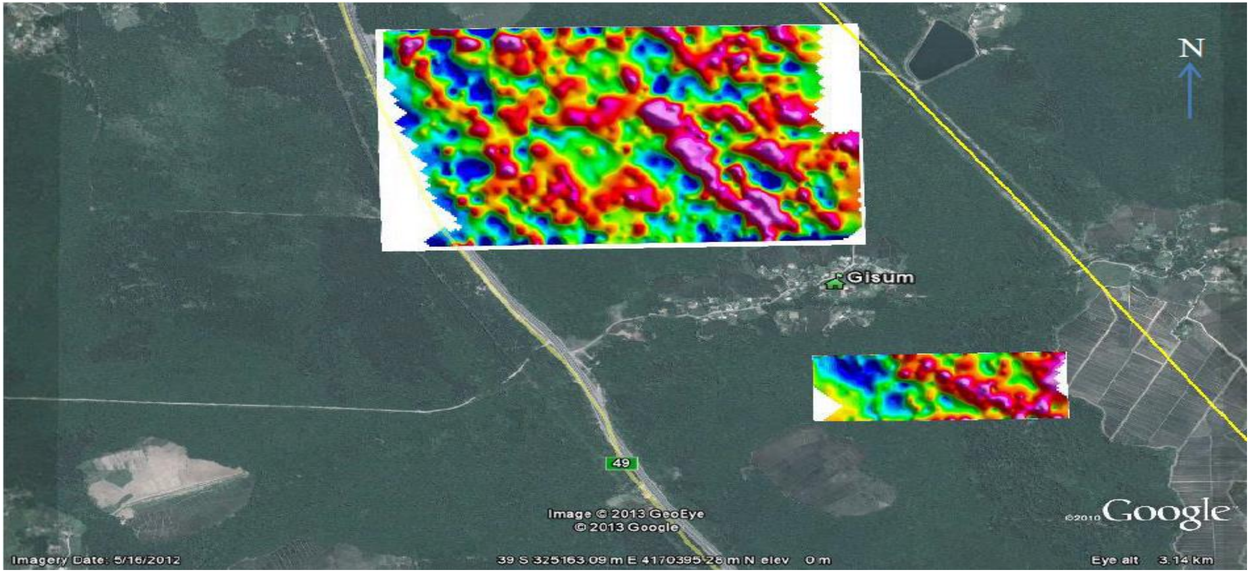

Figure 62: Comparison of magnetic maps in Gisum and the location of magnetic linear trends (Asadi, 2013).

3-5-3-2 Lisar

The studied area is located 27 km north of Talesh city in geographical coordinates 37° 57′ 41″ North and 48° 54′ 25″ East and close to Hareh Dasht village (Figure *63*). The existence of paddy fields and vegetation made it possible to collect only one magnetic profile there. The surveying route was in line with the river and 134 stations were collected in this survey.

Figure 63: The geographic location of the data collection in Lisar area near Hareh Dasht village. The begining and end points of the collection are marked with a white arrow (Asadi, 2013).

In Figure *64* the magnetic anomaly profile is prepared after removing the magnetic field reference. The maximum value of the field is -139, the minimum is -504 and the average is -320 nanotesla, and the difference between the maximum and minimum anomaly is 365 nanotesla. In the surveyed profiles, there are 4 magnetic anomalies with wavelengths of 300 to 500 meters. The range of these anomalies are about 100 to 200 nanotesla. The studied area consists of sandy limestones and andesitic tuffs, which are covered with Quaternary alluvial sediments. In two places, the river displaced right laterally, which could be due to the right-lateral movement of the fault.

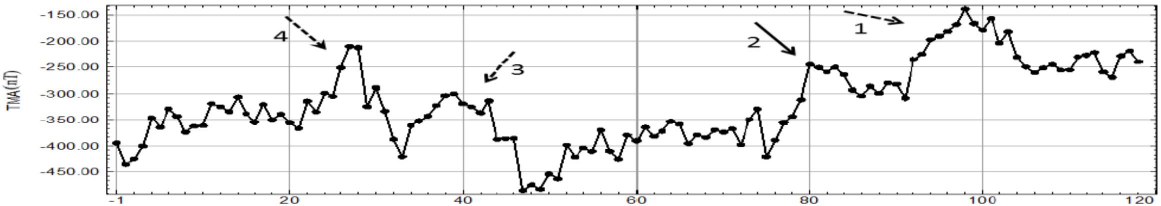

Figure 64: Magnetic field anomaly section carried out in Lisar. The fault locations are shown with arrow number 2 (Asadi, 2013).

The distance between two anomalies 1 and 2 with a length of 500 meters is almost equal to the distance between two anomalies 3 and 4 with a length of 400 meters. In addition, two anomalies (1 and 2) and (3 and 4) are 1500 meters apart and located in the right-lateral displacement of the river. Two anomalies 3 and 4 are coincide with the place of change of two geological units, that is sandstone and andesitic tuffs. Therefore, these anomalies are probably caused by the change of the type of geological units with different magnetic susceptibility and faulting in the area. It is possible that anomalies (1, 2) and (3, 4) are the result of two separate blocks, due to faulting.

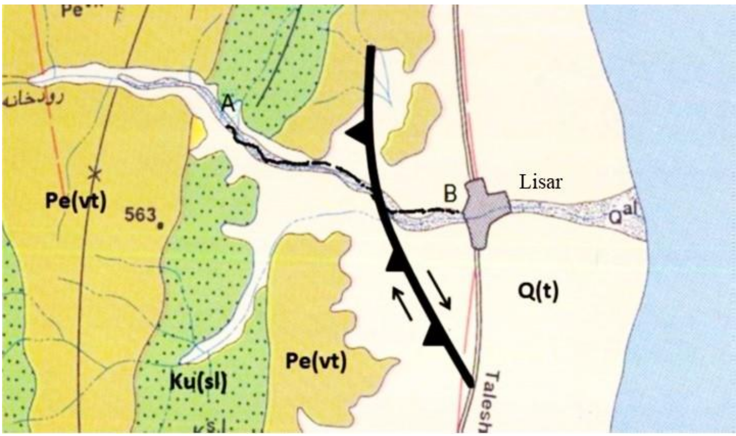

Figure 65: Geological map of the surveyed area. Masured points are marked with a circle along AB line. Q(t): Alluvial sediments and alluvial fan. Ku(sl): Upper Cretaceous limestones. P_e(v.t). : Pliocene

andesitic tuffs. The reverse fault with the strike-slip component is indicated by black lines (Asadi, 2013).

3-5-3-3-Talesh

The studied area is located near the northern suburbs of Talesh city (Figure *66*). The distance between surveying points is 30 meters and the number of surveying points is 136. In this section Data collection has been done in two profiles (Figure *68*). The maximum field is 679 nanotesla, the minimum field is -527 nanotesla and the average field is 5 nanotesla. A shutter ridge with a north-south direction that is parallel to the fault trace is geomorphological evidence of faulting in this area. By studying line number 1, it is possible to see a magnetic anomaly on the eastern side of the mountain slope. The range of this anomaly is about 800 nanotesla, which indicates a structure with a high magnetic susceptibility value (Figure *67*).

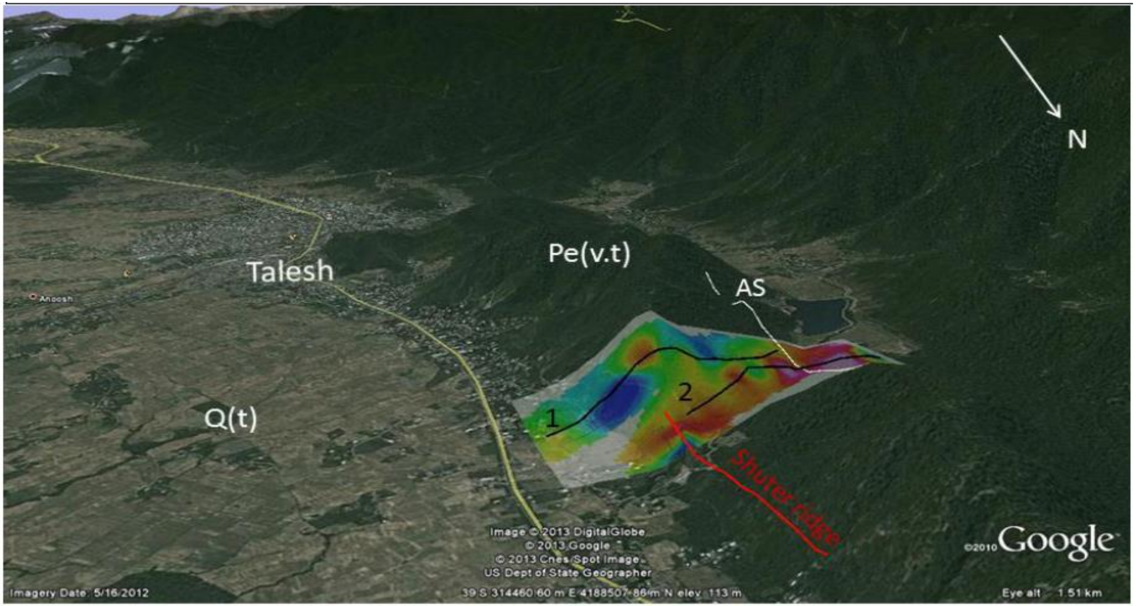

Figure 66: Magnetic anomaly map on the Google Earth image. In this image, the surveying lines are marked in black, the trace of the fault is marked in white, and the shutter ridge is marked in red. Q(t): Quaternary alluvial sediments, Pe (v.t): Andesitic tuffs (Asadi, 2012).

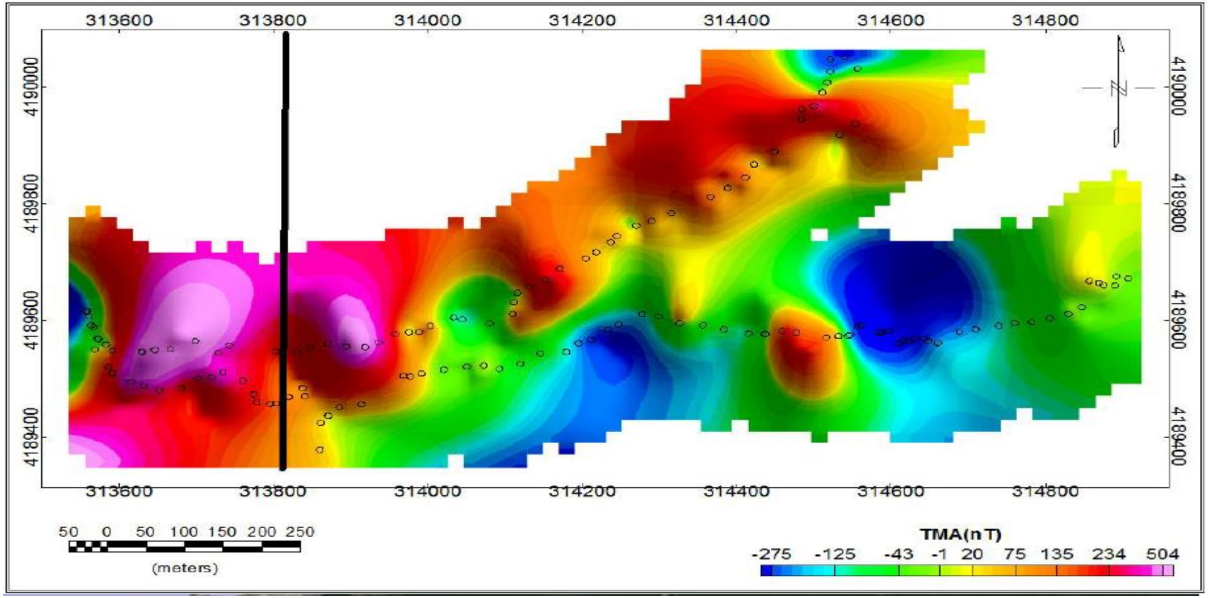

Figure 67: Magnetic anomaly map. The north-south line is the location of the Astara fault (Asadi, 2013).

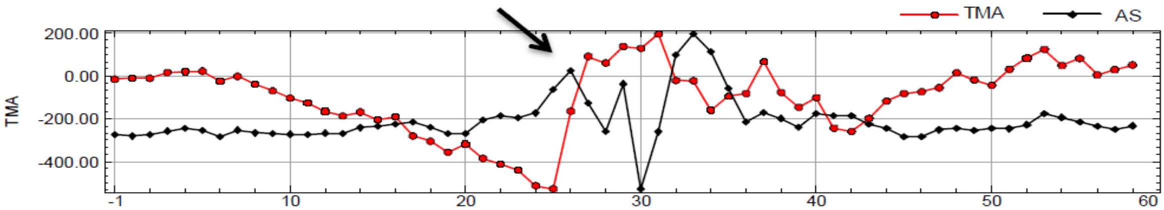

Figure 68: The section of magnetic anomaly in Talash. The arrow shows the location of the shutter ridge (Asadi, 2013).

3-5-3-4 Jokandan

The investigated area is located in Jokandan, near Turk Mahaleh village (10 km north of Talesh city) (Figure *69*). The distance of data collection points is 30 meters and the number of surveying is 718. The minimum value of the field is -538 nanotesla, the maximum value is 562 nanotesla, and the average value is 256 nanotesla. Two anomalies C and D with an amplitude of 500 nanotesla is observed on the both sides of the river and on a hill with a height of about 100 meters. The same amplitude value of these two anomalies can indicate the same geological structure. Along the river, the amplitude of the anomaly in the AB magnetic profile is up to -550 Nanotesla. The hills on the both sides with high magnetic field are composed of andesitic tuffs, and along the river, this unit is covered with Quaternary alluvial sediments.

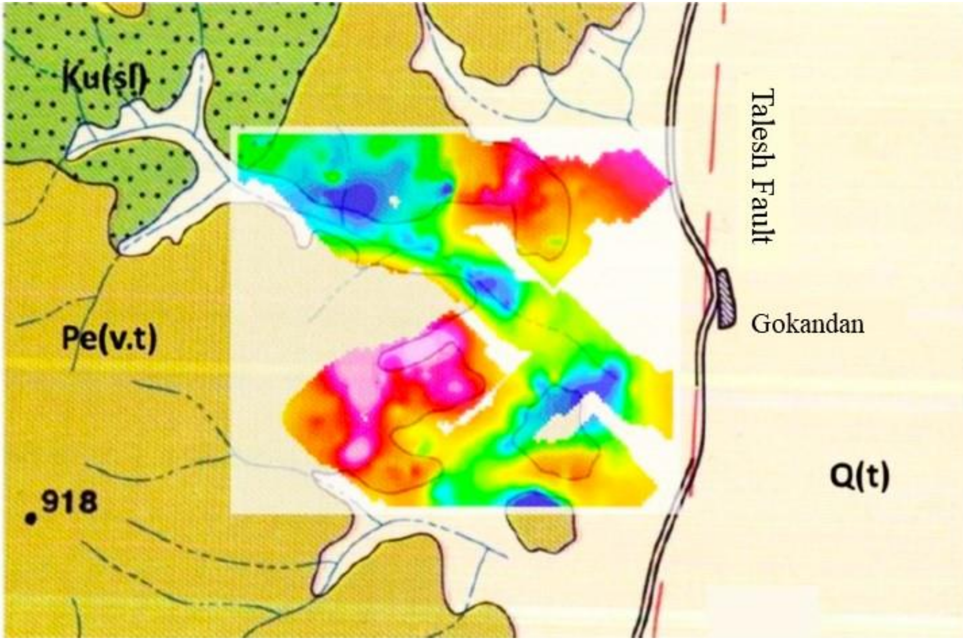

Figure 69: Map of the magnetic field on the geological map of the region. Q(t): Quaternary alluvial sediments, Pe (v.t): Pliocene andesitic tuffs, Ku(sl): Upper Cretaceous sandy limestones (Asadi, 2013).

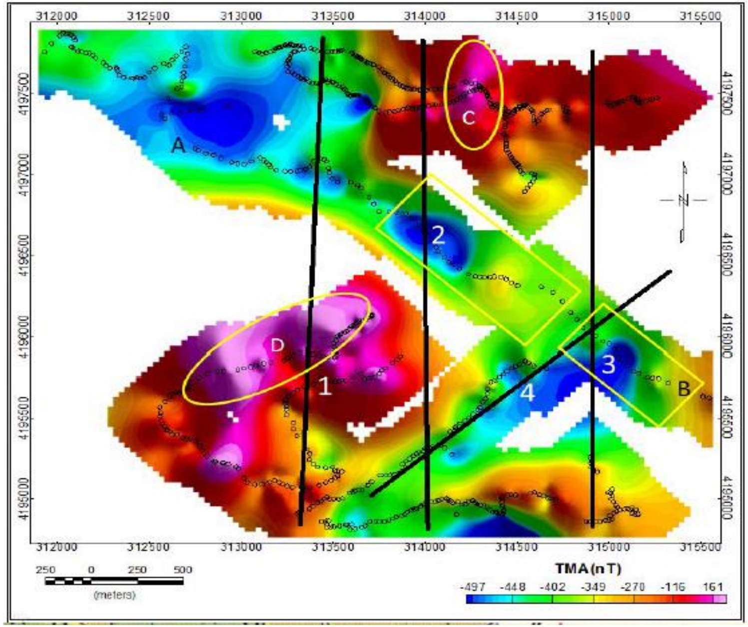

Figure 70: Magnetic anomaly in Jokandan region, surveying points are marked with circles. The black lines from number 1 to 4 are the faults determined by the Geological survey of Iran. The two yellow frameworks are

anomalies suspected to be caused by faults. C and D anomalies with an amplitude of 500 nanotesla can be observed on the both sides of the river and on the hill at a height of 100 meters (Asadi, 2013).

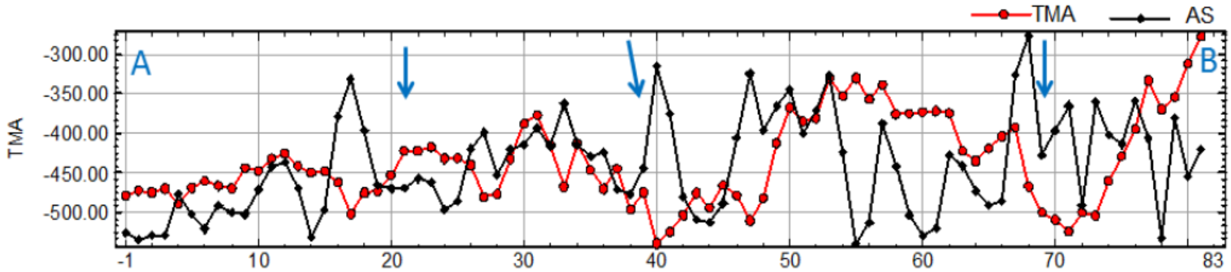

Figure 71: The magnetic anomaly profile of Jokandan, the arrows show the location of the fault (Asadi, 2013).

3-6 Structural analysis of Astara fault

3-6-1 Astara fault geometry

The Astara fault with about 110 km long, in general, constitute of this fault has two trends, i.e. in the northern parts is almost north-south trend and in the southern parts the trend changes and inclines towards the southeast. Due to the trend change, the mechanism of the fault is change and thrust component of the fault increases.

3-6-2 Astara fault mechanism

The present studies, reveals that the Astara fault system consists of two separate components:

1) Astara Thrust Fault (ATF): This segment is the boundary between Talash mountains and the foothills in the east, and consists of three parts. As a result of the activity of this fault, Cretaceous and Paleogene pyroclastic sediments are juxtaposed with Quaternary alluvial sediments.

2) Astara Strike Slip Fault (ASF): This main segment consists of two segments and is located in the western part of the Caspian Sea coast.

CHAPTER FOUR

DISCUSSION and CONCLUSION

4-1 Introduction

In the present research, based on the Hamdouni et. al (2007) methods, active tectonics evaluated in eight basins. When several indices of relative tectonic activity are evaluated for a particular region, it is possible to develop a system of relative tectonic-activity classes. Therefore, on the basis of different indices the area can be divided into three categories: category 1 shows high tectonic activity, category 2 shows medium tectonic activity and category 3 shows low tectonic activity.

4-2 discussion

GPS vectors confirm the dextral component along the Astara fault (Djamour et al., 2010; 2011). This component can also be confirmed by morphotectonic and geophysical investigation. Ritz et al (2006) suggest a clockwise rotation of the South Caspian basin based on tectonic data, especially the data obtained from the changes of the young stress field in Central Alborz. Accordingly, the clockwise rotation of the South Caspian basin causes the left-lateral component on the Caspian fault at the northern edge of the Alborz highlands and the right-lateral component along the Astara fault. The existence of a left-lateral shear mechanism on the Caspian fault and the dextral shear component along the Astara fault system confirmed the correlation of the geodynamic network data of Azerbaijan and Central Alborz (DJamour et al., 2010-2011).

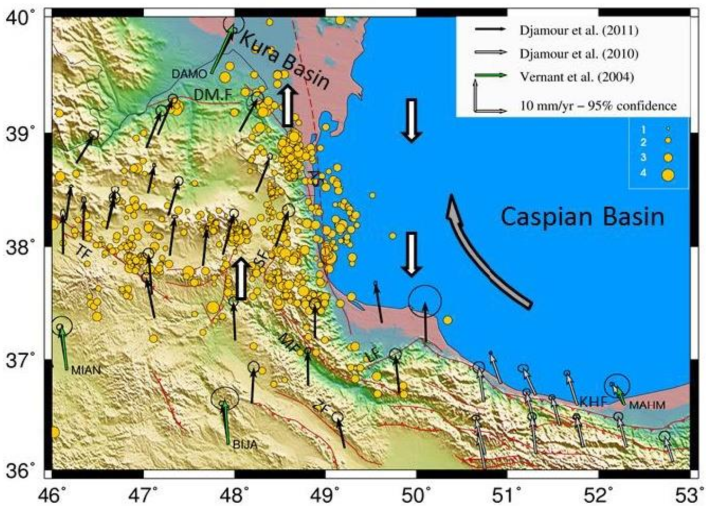

Figure 72: GPS velocity vectors relative to the Eurasian plate on the topography map. White arrows indicate the region with right-lateral movement (Vernant et al., 2004), black arrows show GPS vectors (Djamour et al., 2010; 2011), the gray arrow show the clockwise movement of the South Caspian basin (Ritz et al., 2006).

In this regard, the present research, focusing on the eastern part of Talash mountain by using morphometric data and field observations, try to determine the geometry and mechanism of the Astara fault, especially in the coastal plain. In this section, we will examine and compare the obtained information in different basins:

4-2-1 Morphometric data analysis

4-2-1-1 Basin No. 17: In this basin, the drainage basin shape indices (Bs), hypsometry (Hi) and drainage basin asymmetry factor (AF) are in category 3 of tectonic activity and (i.e low tectonic activity) but the value of transverse topography factor (T) and valley floor width to depth index (V_f) is in category 1, which indicates high tectonic activity. In general, this basin has relatively moderate activity.

4-2-1-2 Basin No. 18: In this basin, B_s, H_i indices are in the 3rd tectonic category, and Vf, AF, and T indices are in the 1st tectonic activity category. In general, the relative tectonic activity of this basin is in category 2, which has high geomorphological activity.

4-2-1-3 Basin No.19: In this basin, Bs, AF and Hi indices are in tectonic activity category 3, and AF index is in category 1 and T index is in tectonic category 2, and in general relative activity of this basin in this region is in the category of moderate geomorphological activity.

4-2-1-4 Basin No.20: B_s and A_f indices in this basin are in tectonic classification 3. V_f and T indices are in tectonic class 1 and hypsometric index is in class 2. In general, the relative activity index in this basin is high.

4-2-1-5 Basin No. 21: In this basin, Bs, AF, Hi indices are in category 3 of tectonic activity, and V_f is in the 1st class and the T index is in the 2nd category, and in general, the relative activity of this basin is in the medium category.

4-2-1-6 Basin No. 22: The activities of this basin are classified as AF, Hi in category 3, Bs index in tectonic class 2 and Vf, T in tectonic category 1 and generally in The tectonic category is in the high activity.

4-2-1-7 Basin No. 23: In this basin, Bs, AF, Hi indices are in tectonic class 3, and Vf and T are in class 1 with high activity, and the relative tectonic activity of this basin is in the medium activity.

4-2-1-8 Basin No. 24: In this basin, Vf, Af, T indices are in tectonic category 1, and Hi and Bs indices are in tectonic categories 2 and 3, respectively, and relative tectonic activity index in this basin is in category 2, which has high activity.

4-3 Conclusion

Based on DEM, IRS and Google Earth satellite images and the calculation of morphometric data, subsurface information processing and field studies along the Astara fault, the following results have been obtained:

1) In terms of geometry, the Astara fault with a length of about 110 km and a gentle slope towards the west, can be followed in the west of Talash mountain. In general, this fault has two trends. in the northern parts, the trend is almost north-south, and in the southern parts inclines towards the southeast. Consequently, the thrust component of faults will be increased.

2) In terms of geomorphology, the Astara fault can be divided into two separate faults, including the Astara thrust fault (ATF), which is located the border of the Talash mountains and the foothills. The Astara thrust fault thrusted Cretaceous and Paleogene pyroclastic sediments from the west over the Quaternary alluvial sediments in the east. Astara strike-slip fault (ASF), is located in the western part of the Caspian Sea coast.

3) The Astara thrust fault consists of three parts, half of the second part and all of the third part is located in the study area of this research, and it continues from Lisar to Shafarood. The maximum and minimum horizontal displacements of the fault in Lisar and Jokandan region is calculated as 1000 and 120 meters

respectively. It is worth to mention that, the maximum horizontal displacement of about 900 meters was measured in Khalaf Abad region and the lowest displacement was 90 meters in Shafarood.

4) In general, all eight studied basins are in category 2 of tectonic activity and are in the medium tectonic class. (Table *9*).

Table 7: The morpho-tectonic information of Astara strike-slip in the study area (Kaveh et al., 2013)

Fault name		Segment	Valley no.	Valley name	Profile	Length (km)	Azimute	GPS (Lat/Lon ddmm'ss" h) Start	GPS (Lat/Lon ddmm'ss" h) End	V (m)	H (m)	H classification	H min-max/ class	H min-max/ segment	Rake/ segment
ASTARA ACTIVE FAULT SYSTEM	Astara Strike Slip Fault (ASF)	1	14	Lisar	1	16.37	269°	37°57' 45.75" 48°45' 1.39"	37°57' 46.70" 48°56' 10.32"	5±2	180±30	A		80-840	1.9°-6.8°
			15	Jokandan	1	15.96	269°	37°55' 23.24" 48°45' 08.2"	37°55' 25.57" 48°55' 52.84"	5±2	110±30	A			
					2	15.95	269°	37°54' 51.72" 48°45' 0.08"	37°54' 54.64" 48°55' 53.58"	10±5	80±30	A			
		2	16	Hashtpar	1	20.89	246°	37°45' 48.48" 48°44' 59.35"	37°50' 21.19" 48°58' 3.98"	5±2	250±30	B	A (70-190) B (200-390) C (500)	70 - 500	0.6°- 4°
					2	21.03	246°	37°45' 35.32" 48°44' 59.35"	37°50' 8.05" 48°45' 8.40"	5±2	260±30	B			
			17	Ali abad	1	21.59	246°	37°42' 34.52" 48°45' 2.66"	37°47' 17.08" 48°58' 34.93"	–	390±30	B			
					2	21.8	246°	37°42' 23.99" 48°45' 1.56"	37°47' 6.55" 48°58' 38.24"	5±2	270±30	B			
					3	22.24	246°	37°41' 49.74" 48°45' 1.56"	37°46' 40.24" 48°58' 52.61"	10±5	340±30	B			
					4	22.47	246°	37°41' 13.74" 48°45' 2.66"	37°46' 8.66" 48°59' 13.61"	5±2	500±30	C			
			18	Khalaf abad	1	27.11	232°	37°36' 30.47" 48°44' 59.95"	37°45' 33.67" 48°59' 43.25"	–	90±30	A			
					2	27.52	232°	37°36' 22.10" 48°44' 58.78"	37°45' 27.18" 48°59' 44.41"	5±2	120±30	A			
					3	27.39	232°	37°35' 32.83" 48°44' 55.27"	37°44' 38.01" 48°59' 39.74"	5±2	250±30	B			
					4	27.41	232°	37°35' 24.47" 48°45' 4.62"	37°44' 26.88" 48°59' 39.74"	–	230±30	B			
					5	26.05	242°	37°36' 42.55" 48°45' 2.28"	37°43' 14.50" 49°00' 33.49"	5±2	70±30	A			
			19	Gisoum	1	28.69	242°	37°34' 17.05" 48°44' 59.55"	37°41' 31.95" 49°02' 15.97"	30±5	250±30	B			
					2	30.65	242°	37°32' 42.31" 48°44' 59.55"	37°40' 27.30" 49°03' 26.78"	40±5	200±30	B			
			20	Molla mahale	1	22.12	217°	37°30' 7.03" 48°55' 19.50"	37°39' 29.02" 49°04' 24.40"	5±2	110±30	A			
					2	21.6	221°	37°30' 0.38" 48°55' 43.13"	37°38' 45.92" 49°05' 14.44"	10±5	190±30	A			
					3	21.7	226°	37°30' 0.38" 48°55' 37.57"	37°37' 58.38" 49°06' 23.94"	10±5	350±30	B			
					4	17.92	219°	37°29' 50.41" 48°59' 24.15"	37°37' 18.58" 49°07' 9.81"	10±5	120±30	A			
					5	16.95	219°	37°29' 58.17" 49°00' 15.58"	37°37' 0.89" 49°07' 33.45"	5±2	190±30	A			
			22	Shafa roud	1	14.5	221°	37°30' 0.41" 49°02' 53.33"	37°35' 53.33" 49°09' 25.72"	10±5	320±30	B			
					2	11.99	221°	37°30' 2.06" 49°05' 30.08"	37°34' 52.20" 49°10' 57.08"	5±2	180±30	A			

*V: Vertical offset,, **H:** Horizental offset,, **H classification:** A(<200m), B(200-400m), C(400-600m), D(600-800m), E(≥800m)*

Table 8: The morpho-tectonics data of the Astara thrust fault in the study area (Kaveh et al., 2013)

Fault name		Segment	Valley no.	Valley name	Profile	Length (km)	Azimute	GPS (Lat/Lon ddmm'ss" h) Start	GPS (Lat/Lon ddmm'ss" h) End	V (m)	H (m)	H classification	H min-max/ class	H min-max/ segment	Rake/ segment
ASTARA ACTIVE FAULT SYSTEM	Astara Thrust Fault (ATF)	2	14	Lisar	1	15.97	270°	37°58' 6.82" 48°45' 0.92"	37°57' 56.69" 48°55' 56.40"	130±30	1000±30	E	D (650-680) E (860-1000)	90-1000	5.7°-7.2°
					2	15.97	270°	37°57' 44.04" 48°45' 1.98"	37°57' 36.44" 48°55' 57.47"	100±30	570±30	C			
					3	15.97	270°	37°56' 38.21" 48°45' 0.92"	37°56' 37.37" 48°56' 1.73"	10±5	140±30	A			
			15	Jokandan	1	15.93	270°	37°54' 39.19" 48°45' 0.92"	37°54' 40.02" 48°55' 53.20"	40±5	570±30	C			
					2	15.93	270°	37°54' 17.22" 48°45' 1.98"	37°54' 16.37" 48°55' 53.20"	10±5	590±30	C			
					3	15.93	270°	37°53' 45.97" 48°45' 1.98"	37°53' 45.12" 48°55' 54.27"	50±5	860±30	E			
					4	16.13	270°	37°53' 42.59" 48°45' 1.98"	37°53' 41.74" 48°56' 1.73"	45±5	680±30	D			
					5	16.38	270°	37°53' 2.89" 48°45' 0.92"	37°53' 2.89" 48°56' 13.45"	90±30	650±30	D			
					6	16.67	270°	37°52' 40.08" 48°45' 1.98"	37°52' 40.08" 48°56' 26.24"	40±5	340±30	B			
					7	17.11	270°	37°52' 24.03" 48°45' 0.92"	37°52' 22.34" 48°56' 42.23"	30±5	120±30	A			
			16	Hashtpar	1	19.61	270°	37°49' 16.40" 48°45' 1.98"	37°49' 16.40" 48°58' 22.42"	35±5	140±30	A			
					2	19.61	270°	37°48' 56.11" 48°45' 0.92"	37°48' 56.11" 48°58' 24.55"	50±5	220±30	B			
					3	19.62	270°	37°47' 53.53" 48°45' 1.98"	37°47' 51.84" 48°58' 23.48"	30±5	180±30	A			
					4	19.62	270°	37°47' 33.23" 48°45' 3.05"	37°47' 33.23" 48°58' 25.62"	65±30	340±30	B			
		3	17	Ali abad	1	20.74	270°	37°46' 5.26" 48°45' 3.05"	37°46' 6.10" 48°59' 11.45"	25±5	240±30	B	A (90-130) B (240-320) C (400-590) D (690) E (860-900)	90 - 900	6.3° - 11.9°
					2	21.9	245°	37°42' 48.89" 48°45' 1.98"	37°47' 48.46" 48°58' 30.95"	20±5	410±30	C			
					3	21.9	245°	37°42' 5.71" 48°45' 5.18"	37°47' 7.86" 48°58' 34.14"	45±5	240±30	B			
			18	Khalaf abad	1	23	270°	37°43' 10.06" 48°45' 4.12"	37°43' 7.52" 49°00' 43.11"	90±30	460±30	C			
					2	23.85	244°	37°38' 43.24" 48°44' 58.79"	37°44' 14.40" 48°59' 51.95"	95±30	690±30	D			
					3	24.54	245°	37°37' 43.90" 48°45' 0.92"	37°43' 26.99" 49°00' 27.12"	20±5	900±30	E			
					4	26.03	245°	37°36' 25.91" 48°45' 3.05"	37°42' 23.49" 49°01' 16.15"	45±5	400±30	C			
			19	Gisoum	1	29.46	245°	37°33' 53.02" 48°45' 4.12"	37°40' 33.60" 49°03' 14.46"	30±5	300±30	B			
					2	30.32	245°	37°32' 59.57" 48°45' 2.52"	37°39' 56.75" 49°03' 54.42"	20±5	320±30	B			
					3	31.64	242°	37°31' 44.46" 48°45' 4.12"	37°39' 38.95" 49°04' 15.21"	30±5	250±30	B			
			20	Molla mahale	1	22.17	224°	37°30' 0.01" 48°55' 19.94"	37°38' 23.87" 49°05' 45.04"	10±5	270±30	B			
					2	20.48	224°	37°29' 58.96" 48°56' 53.57"	37°37' 48.21" 49°06' 32.52"	10±5	240±30	B			
					3	19.18	224°	37°30' 1.06" 48°57' 56.87"	37°37' 24.09" 49°07' 6.81"	10±5	590±30	C			
					4	18.47	224°	37°30' 0.01" 48°58' 40.39"	37°37' 6.26" 49°07' 29.23"	10±5	470±30	C			
			21	Kaliman	1	17.19	224°	37°30' 1.06" 49°00' 44.36"	37°36' 20.09" 49°08' 35.17"	10±5	860±30	E			
			22	Shafa roud	1	15.42	224°	37°30' 0.01" 49°02' 8.76"	37°35' 49.67" 49°09' 22.64"	–	220±30	B			
					2	14.56	222°	37°29' 57.62" 49°02' 55.53"	37°35' 42.12" 49°09' 38.49"	15±5	130±30	A			
					3	13.37	221°	37°29' 56.92" 49°04' 8.08"	37°35' 24.04" 49°10' 5.58"	10±5	90±30	A			
					4	11.56	221°	37°29' 56.92" 49°06' 34.05"	37°34' 31.17" 49°11' 36.49"	–	460±30	C			

Table 9: Result of the morphometry indices of all basins (Kaveh et al., 2013)

Morphometry Index of the Talesh Mountain Basins

Basins	Bs	Tectonic Class	Vf	Tectonic Class	AF	Tectonic Class	Hi	Tectonic Class	T	Tectonic Class	Smf/segment	Tectonic Class	Value Iat	Class Iat	References
1	2.44	3 (Low Activity)	0.234	1 (High Activity)	51.62%	3 (Low Activity)	0.249	3 (Super Mature)	0.027	3 (Low Activity)			2.66	3	
2	3.86	2 (Moderate Activity)	0.26	1	40.69%	2 (Moderate Activity)	0.341	3	0.071	2 (Moderate Activity)	3.1	3 (Low Activity)	2.16	2	
3	2.83	3	0.238	1	45.35%	3	0.3	3	0.334	1 (High Activity)			2.33	2	
4	3.45	2	0.201	1	33.83%	1 (High Activity)	0.329	3	0.085	2			1.83	1	
5	3.09	2	0.244	1	58.20%	2	0.429	2 (Mature)	0.054	2			1.83	1	
6	3.79	2	0.217	1	59.72%	2	0.347	3	0.092	2			2	2	Air photo, 1955. Bull, 2007. DEM 30m. El Hamdouni et al., 2008. Geological map of Ardabil; 1:250000 , GSI. Geological map of Bandar-e-Anzali; 1:250000 , GSI. Geological map of Astara; 1:100000 , GSI. Geological map of khalkhal - Rezvanshahr; 1:100000 ,GSI. Google Earth. IRS Images, 5m. Keller & Pinter, 2002. Seismotectonic map of NW Iran; 1:750000 ,GSI. Silva et al., 2003.
7	3.154	2	0.253	1	48.70%	3	0.422	2	0.049	3			2.16	2	
8	3.97	2	0.273	1	65.25%	1	0.442	2	0.285	1			1.5	1	
9	2.367	3	0.635	2	34.93%	1	0.352	3	0.394	1			2	2	
10	3.33	2	0.276	1	42.00%	2	0.387	3	0.399	1			1.83	1	
11	5.348	1 (High Activity)	0.188	1	39.62%	2	0.407	2	0.195	1	2.74	2 (Moderate Activity)	1.5	1	
12	2.84	3	0.223	1	65.04%	1	0.358	3	0.307	1			1.83	1	
13	4.28	1	0.348	1	49.72%	3	0.4	2	0.068	2			1.83	1	
14	1.55	3	0.223	1	52.28%	3	0.401	2	0.056	2			2.16	2	
15	3.9	2	0.26	1	60.57%	2	0.341	3	0.198	1			1.83	1	
16	2.38	3	0.14	1	50.75%	3	0.459	2	0.109	1			2	2	
17	1.581	3	0.454	1	51.54%	3	0.372	3	0.358	1			2.16	2	
18	1.94	3	0.21	1	60.60%	2	0.299	3	0.265	1			2	2	
19	1.16	3	0.41	1	47.84%	3	0.355	3	0.054	2			2.33	2	
20	2.22	3	0.289	1	53.54%	3	0.406	2	0.343	1			2	2	
21	1.358	3	0.342	1	53.98%	3	0.306	3	0.077	2			2.33	2	
22	3.92	2	0.172	1	47.79%	3	0.364	3	0.135	1	2.05	2	2	2	
23	2.56	3	0.19	1	47.56%	3	0.3436	3	0.345	1			2.16	2	
24	2.409	3	0.116	1	56.33%	3	0.424	2	0.549	1			2	2	

***Bs:** Drainage Basin shape,, **Vf:** Ratio of Valley floor width to valley height,, **AF:** Asymmetry Factor,, **Hi:** Hypsometric Integral,, **T:** Transverse topographic symmetry factor,, **Smf:** Mountain Front Sinuosity,, **Iat:** Index of active tectonic*

Table 10: The final information on the geometry of Astara fault (Kaveh et al., 2013)

ASTARA ACTIVE FAULT SYSTEM															
Fault name	Segment	Length (km)	Azimute	Dip	Mechanism	H (m)		V (m)		Rake/ segment	Slip Rate (mm/yr)	Earthquake Related		References
						H min	H max	V min	V max			Instrument	Historical	
Astara Thrust Fault (ATF)	1	≤13	346°	70° - 80°	Strike slip (right lateral), Thrust	190	1500	10	15	0.3° - 4°	~ 1.5	24-06-1903; mb=5.5 (AMB) 24-06-1907; ms=5.9 (AMB) 11-07-1970; mb=5.2 (EHB) 4-11-1978; mw=6.3 (EHB) 4-05-1980; mw=6.5 (EHB) 5-11-2006; mn=5 (ISC) 23-03-2008; mn=5 (ISC)	1709 AD ?? 1713 AD ??	Air photo, 1955. Ambraseys & Melville, 1982. DEM 30m. Geological map of Ardabil; 1:250000 , GSI. Geological map of Bandar-e-Anzali; 1:250000 , GSI. Geological map of Astara; 1:100000 , GSI. Geological map of khalkhal - Rezvanshahr; 1:100000 ,GSI. Google Earth. IRS Images, 5m. McCalpin, 2009. Nazari, 2006. Seismotectonic map of NW Iran; 1:750000 ,GSI.
	2	≤63	354°	80° - 90°	Strike slip (right lateral), Thrust	90	1000	10	130	5.7° - 7.2°				
	3	≤32	322°	60° - 70°	Thrust, Strike slip (right lateral)	90	900	10	95	6.3° - 11.9°				
Astara Strike slip Fault (ASF)	1	≤40	356°	80° - 90°	Strike slip (right lateral)	80	840	5	30	1.9° - 6.8°				
	2	≤24	316°	60° - 70°	Thrust, Strike slip (right lateral)	70	500	5	40	0.6° - 4°				

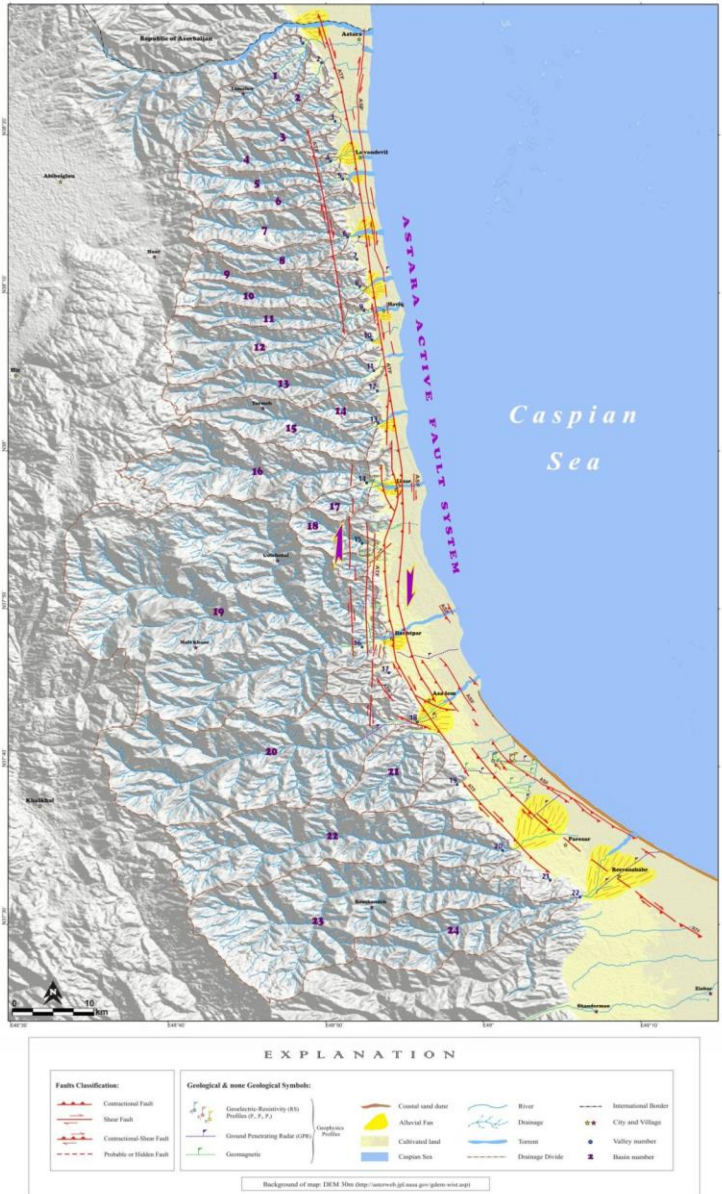
Republic of Azerbaijan
Astara
Caspian Sea
ASTARA ACTIVE FAULT SYSTEM
0 10 km
EXPLANATION
Faults Classification:
Contractional Fault
Shear Fault
Contractional-Shear Fault
Probable or Hidden Fault
Geological & none Geological Symbols:
Geoelectric-Resistivity (RS) Profiles
Ground Penetrating Radar (GPR)
Geomagnetic
Geophysics Profiles
Coastal sand dune
Alluvial Fan
Cultivated land
Caspian Sea
River
Drainage
Torrent
Drainage Divide
International Border
City and Village
Valley number
Basin number
Background of map: DEM 30m

Figure 73: Geomorphological map of Astara fault (Kaveh et al., 2013)

4.4 Suggestions

1) In order to know the progressive zones of the Astara fault in the Caspian, it is necessary to carry out seismic and sonar profiles perpendicular to the Astara fault (east-west).

2) Paleoseismological studies will help for seismic hazard evaluation in the area.

3) Considering the thick forest cover of the Talash mountains and the coastal plain, using imaging methods such as LIDAR sensors will be useful in knowing as much as possible the active structures hidden in the forest zones.

References

Alavi, M., 1996.Tectonostratigraphic synthesis & structural style of the Alborz mountain system in northern Iran,Journal of Geodynamics V.21,p.1-33

Allen, M.B., Gassemi, M.R., Shahrabi, M., & Ghorashi, M., 2003.Accommodation of late Cenozoic oblique shortening in the Alborz range,northern Iran.J.Struc.Geol., V.25 p.659-672

Asadi, V., (2013), Identification of Astara active fault using geoelectrical and geomagnetic methods, MSc, Gavazang-Zanjan University of Basic Sciences.

Bull, W.B.2007, Tectonic geomorphology of mountains:A new approach to paleoseismology . Black well publishing.136 P.

Burbank, DW., Anderson, R.G., 2001.Tectonic Geomorphology. Black Weel Science,Massachusetts

Djamour, Y., Vernant, P., Bayer, R., Nankali, H., Ritz, J.F., Hinderer, J., Hatam, Y., Luck, B., Le Moigne, N., Sedighi, M., Khorrami, F., 2010. GPS and gravity constraints on continental deformation in the Alborz Mountain range, Iran. Geophysical Journal International 183, 1287–1301.

Djamour, Y., Vernant, P., Nankali, H.R., Tavakoli, F., 2011. NW Iran-eastern Turkey present-day kinematics: results from the Iranian permanent GPS network. Ea

Ghorashi, M., Arin, M., (2010) Tectonics of Iran, Moraba Abi Publications. 312 p.

Gourabi, A., (2005), Geomorphological evidences of active tectonics of Darakeh basin. No. 60, pp. 177-196.

Hamdouni, R.EI., Irigaray, C., Fernandez, T., Chacon, J., Keller, E.A., 2007.Assessment of relative active tectonics, southwest border of sierra Nevada (southern Spain). Geomorphology 96,150-173

Jackson, J.A., Priestley, K., Allen, M.B., Berberian, M., 2002.Active tectonics of the South Caspian Basin.Geophysical Journal International.V.148, p.214-245

Keller, E.A., Pinter.N., 1996.Active tectonics:Earthquake ,uplift and landscape ,Prentice –Hall Inc.New Jersey.Second edition.338p.

Keller, E.A., Pinter.N., 2002.Active tectonics:Earthquake ,uplift and landscape

,Prentice –Hall Inc.New Jersey.Second edition.362p.

Lowrie W., 2007. Fundamentals of geophysics, Cambridge University Press, 1st edition, 392p.

Mohammadi Vizheh, M., (2013), Geophysical studies using GPR method to identify active faults and study sedimentology in Gilan province, Directorate of Regional Exploration of Geophysics Department, Geological Survey of Iran, 123 p.

Nazari, H., Shahidi, A., (2011), Tectonic of Iran (Alborz). Geological Survey of Iran, Earth Sciences Research Institute. Tehran: Javan Emroz. 164 p.

Nazari, H.,2006-Analyse de la tectinique recente et active dans l̕Alborz Central et la region de Tehran:approche morphotectonique et paleoseismologique,Ph,D, thesis.University if Montpellier Π ,Montpellier,France.247.

Razavi, A., (2013), Geophysical report using RS method to study the fault zone of Gilan province Gisum region. 39 p.

Ritz, F., Nazari.H., 2006-Active transtention inside central Alborz:a new insight into the Northern Iran-Southern Caspian geodynamics,Geology.34.P3477-480.

Stampfli, G.,1996-The Intra –Alpine terrain:a Paleotethyan remnant in the Alpine Variscides.Ecologae geologicae Helvetiae ,89,13-42.

Stocklin, J.,1974-Northern Iran:Alborz mountains Geol.Sol.Lon.Spacial Pub. No .4 P.213-334

Tatar, M.,2001-Etude Seismotectonique de deux zones de collision continental le Zagros le central et l'Alborz, Iran,PhD thesis ,University de Joseph Fourier.

Tchalenko, J. S., Berberian, M., Iranmanesh, H., Bailly, M., and Arsovsky, M. 1974, Tectonic framework of the Tehran region. In: Materials for the study of seismotectonics of Iran; North-central Iran. Geol. Surv. Iran. 29, 7-46.

Vernant,Ph.et al.,2004-Contemporary crustal deformation and plate kinematics in Middle East constrained by GPS measurements in Iran and northern Oman.Geophys.J.Int. 157,P.381-398.

Zanchi, Brea, Mattei., Gassemi, M.R., Sabouri, J.,2006-Inversion tectonic in central Alborz,Iran.J.Structural Geology.15,P.